1	Scattering Properties and Lidar Characteristics of Asian Dust Particles Based on Realistic	Deleted: properties
2	Shape Models	
3		
4	To be submitted to ACP	
5	Anthony La Luna ^{1,2} , Zhibo Zhang ^{1,2*} , Jianyu Zheng ^{2,3} , Qianqian Song ¹ , Hongbin Yu ³ , Jiachen	Deleted: ² ,
6	Ding ⁴ , Ping Yang ⁴ , Masanori Saito ⁵	Formatted: No underline, Font color: Auto
"	Ding, Ting Tang, Masanon Salto	Formatted: No underline, Font color: Auto Formatted: Not Superscript/ Subscript
7	1. Physics Department, University of Maryland Baltimore County (UMBC), Baltimore,	Formatted: Not superscript subscript Formatted: No underline, Font color: Auto
8	MD, USA	Formatted: Outline numbered + Level: 1 + Numbering Style: 1, 2, 3, + Start at: 1 + Alignment: Left + Aligned at: 0.25" + Indent at: 0.5"
9	2. Goddard Earth Sciences Technology and Research (GESTAR) II, UMBC, Baltimore,	
10	MD, USA	
11	3. NASA Goddard Space Flight Center Greenbelt, MD USA	
12	4. Texas A&M University, College Station, TX, USA	
13	5. University of Wyoming, Laramie, WY, USA	
14	Correspondence to: Zhibo Zhang zzbatmos@umbc.edu	Formatted: No underline, Font color: Auto

18 Abstract Formatted: Font: Times New Roman 19 The lidar backscattering properties of Asian dust particles, namely the lidar ratio (S) and Formatted: Font: Cambria Math 20 backscattering depolarization ratio (δ) , were studied using a discrete dipole approximation Deleted: δ (DDA) model. The three-dimensional morphology of the dust particles was reconstructed in fine 21 22 detail using the focused ion-beam (FIB) tomography technique. An index based on the symmetry 23 of the scattering matrix was developed to assess the convergence for the random orientation Deleted: phase Deleted: of conditionusing DDA. Both the S and δ exhibit an asymptotic trend with dust particle size: the S24 Deleted: computation using Deleted: δ initially decreases while the δ increases with size, before both approach their asymptotic values. 25 Formatted: Font: Cambria Math Formatted: Font: Cambria Math 26 The lidar properties were found to have statistically insignificant dependence on effective Deleted: δ sphericity. The presence of strongly absorbing minerals, such as magnetite, can greatly reduce Commented [Z1]: we can explain this in the text not need for abstract/ 27 28 the dust's single-scattering albedo and δ . Utilizing the robust asymptotic trend behavior, two Deleted: δ 29 parameterization schemes were developed: one to estimate the δ of a single dust particle given Deleted: δ its size, and the other to estimate the δ of polydisperse dust particles with a lognormal particle 30 Deleted: δ 31 size distribution given the effective radius. The parameterization scheme was compared with results based on the TAMUdust2020 database, showing that hexahedralsreasonably represent 32 Deleted: hexahedrals to reasonably 33 realistic particle geometries for light-scattering computations. Deleted: with similar physical properties

3435

Formatted: Header

1. Introduction

Dust aerosols are an important component of the Earth System, interacting with Earth's energy, water, and carbon cycles. Directly, dust aerosols scatter and absorb both shortwave and longwave radiation, influencing the planet's energy balance (Tegen et al., 1996; Miller and Tegen, 1998; Myhre et al., 2013; Song et al., 2018, 2022). By scattering incoming solar radiation, dust aerosols contribute to cooling the atmosphere and surface regionally, impacting temperatures and affecting atmospheric circulation patterns (Evan et al., 2006; Lau and Kim, 2007; Zhang et al.,

54 2022

55

56

57

58

59

60

61

62

63

64

65

47

48

49

50

51

52

53

The transport of dust aerosols also has far-reaching implications. The long-range transport of Asian dust is frequently observed on the United States' west coast with considerable impacts on the air quality and climate (Yu et al., 2012; Creamean et al., 2014; Wu et al., 2015). It is also observed impacting Taiwan through similar transport mechanisms (Lin et al., 2007). In fact, mineral dust from the Taklimakan desert has been found to be transported a full rotation around the globe (Uno et al., 2009). Moreover, the deposition of dust aerosol during the long-range transport brings essential nutrients such as iron and phosphorus from terrestrial sources to marine ecosystems, being part of biogeochemical cycles across vast distances (Baker et al., 2003; Yu et al., 2015b; Westberry et al., 2023). Asian dust deposition in the East China Sea stimulates phytoplankton growth and primary productivity, influencing marine food webs and carbon cycling (Kong, S. S.-K. et al., 2022).

66 67

68

69

Lidar is an important tool for remote sensing measurements of airborne dust particles. As demonstrated in many previous studies (Omar et al., 2009; Burton et al., 2012), it allows us to

Formatted: Outline numbered + Level: 1 + Numbering Style: 1, 2, 3, ... + Start at: 1 + Alignment: Right + Aligned at: 0.25" + Indent at: 0.5"

Commented [Z2]: Not sure this is a classic paper.
There are a few high-impact papers on dust influences on tropical cyclone genesis

Evan et al. 2006

https://agupubs.onlinelibrary.wiley.com/doi/full/10.1029/2006GL026408

Lau and Kim 2007 https://agupubs.onlinelibrary.wiley.com/doi/full/10.1029 2007GL031538

Deleted:). For example, Asian dust transportation to the Tibetan Plateau causes direct radiation effects which result in enhancement to the monsoon season (Lau et al., 2006). In addition, the absorption of longwave radiation, particularly thermal infrared radiation, by dust particles leads to surface warming effect by 0.54 W m⁻² on a global average (Song et al., 2022). Indirectly, dust aerosols serve as nuclei for cloud condensation and ice nucleation, altering cloud microphysical properties and precipitation patterns (Atkinson et al., 2013; Field et al., 2006; Kanji et al., 2017). These indirect effects can further influence regional and global climate dynamics by modifying cloud albedo and distribution (Johnson et al., 2004; Huang et al., 2006; Helmert et al., 2007; Amiri-Farahani et al., 2019).

Formatted: Strikethrough

Deleted: this

Deleted: facilitating the working

and study their evolution as they interact with the environment such as clouds, atmospheric gases, and other aerosols. Among others, elastic backscattering lidars are one of the most widely used types of lidar. For example, Cloud-Aerosol Lidar and Infrared Pathfinder Satellite Observations (CALIPSO), is a NASA-French satellite mission that implements a two-wavelength elastic lidar Cloud-Aerosol Lidar with Orthogonal Polarization (CALIOP) at 532 nm and 1064 nm wavelengths (Winker et al., 2009). Ground-based lidar networks such as the NASA Micro-Pulse Lidar Network (MPLNET) use single wavelength measurements for extinction, backscattering, and depolarization profiles (Welton et al., 2001). The EarthCARE mission utilizes ATmospheric LIDar (ATLID), a 355 nm wavelength laser and high-spectral resolution receiver, allowing it to directly measure both lidar ratio and extinction coefficient (Illingworth et al., 2015; Donovan et al., 2024). Ground based lidars operating at 532 nm and

1064 nm throughout Eastern Asia are also useful for monitoring dust transport and air quality,

running as part of Asian Development Bank (ADB) and Global Environment Facility (GEF)

distinguish dust aerosols from clouds and other types of aerosols, track their long-range transport

Deleted: gasses

2. Theoretical Background

(Sugimoto et al., 2008).

Lidar ratio (S) and depolarization ratio (S) are two most important parameters for lidar-based remote sensing of aerosols and clouds. For a single dust particle, the S, referred to as the extinction-to-backscatter coefficient, is defined as (Platt, 1979; Ansmann et al., 1992; Mattis et al., 2002; Liu et al., 2002)

Deleted: δ

Formatted: Font: Cambria Math

Formatted: Font: Cambria Math

 $S = \sigma/\beta = \frac{4\pi}{\omega P_{11}(\theta_s = \pi)},\tag{1}$

where φ is the extinction coefficient and ω and P_{11} are the single-scattering albedo and phase

function of the dust particle, respectively. For the purposes of this paper, P_{11} is normalized to 1

when integrating across all scattering directions $\beta = P_{11}(\theta_s = \pi)C_{sca}$ is the backscattering

coefficient at the exact backscattering direction. When considering a multitude of particles,

$$\beta = \int_{-\infty}^{\infty} P_{11}(r_v, \theta_s = \pi) C_{sca}(r_v) n(r_v) d\ln r_v, \qquad (2)$$

Where r_v is the volume-equivalent sphere radius and $n(r_v) = dN/dlnr_v$ defines a normalized

particle size distribution $(n(r_v))$.

110

111

112

113

115

116

117

119

120

122

123

125

126

127

129

For Raman lidar and high spectral resolution lidar systems, the lidar ratio can be derived directly

118 from the observed extinction and backscatter without assumptions about the composition (Müller

et al., 2007). However, for elastic backscattering lidars, the lidar ratio cannot be directly

measured. As a result, assumptions need to be made about the composition of the atmosphere.

Therefore, the lidar ratio is fundamentally important for elastic lidars like CALIOP and

MPLNET to convert the direct attenuated backscatter observations to an extinction profile

(Young et al., 2018) and derived quantities such as dust aerosol optical depth (Yu et al., 2015a;

124 Song et al., 2021).

Depolarization ratio δ is the ratio of the perpendicular or cross-polarized component to the

parallel component of polarized backscattering signal. For backscattering lidar the

128 depolarization ratio is defined as

Deleted: $S = \sigma/\beta = \frac{4\pi}{\omega P_{11}(\theta_s = \pi)}$,

Formatted: Font: Cambria Math

Formatted: Line spacing: Multiple 1.15 li

Formatted Table

Deleted: σ

Deleted: ω

Deleted: bulk optical properties of polydisperse dust particles, the ...

Commented [4]: Csca here is the scattering cross section, but it should be the scattering coefficient. The units are not correct if you use the scattering cross section.

Commented [5]: Is the equation of backscattering coefficient correct? The unit should be [m-1 sr-1], right? But in your equation, the unit is [m2] @alaluna1@umbc.edu

Deleted: β

Deleted: $(\theta_s = \pi)$

Deleted: ; defined for

Deleted: normalized particle size distribution as

Commented [6]: This equation of beta makes more sense to me, but still the unit is [m-1], could you check if a 1/(4*pi) was missed at the beginning?
@alaluna1@umbc.edu

Deleted: $\beta = \int_{-\infty}^{\infty} P_{11}(r_v, \theta_s = \pi) C_{sca}(r_v) n(r_v) d \ln r_v$

Formatted Table

Deleted: it

Commented [Z7]: Spell out acronyms when used for the first time

Deleted: δ

 $= \frac{1 - \frac{P_{22}(\theta_s = \pi)}{P_{11}(\theta_s = \pi)}}{1 + \frac{P_{22}(\theta_s = \pi)}{P_{21}(\theta_s = \pi)}}$ (3)

Deleted: $\delta = \frac{1 - \frac{P_{22}(\theta_s = \pi)}{P_{11}(\theta_s = \pi)}}{1 + \frac{P_{22}(\theta_s = \pi)}{P_{12}(\theta_s = \pi)}}$

Formatted Table

Deleted: phase

Therefore, δ

where P_{ij} is the ij-th element of the particle's scattering matrix (Kong, S. et al., 2022). δ is often

142

143

144

145

146

147

148

149

150

151

152

154

155

156

157

158

159

160

161

162

used for aerosol type (Kim et al., 2018) and cloud phase classifications (Hu et al., 2009). First,

if lidar backscattering is dominated by single scattering, δ is close to zero for spherical particles

like sulfate aerosols and water droplets. In contrast, δ is notably greater for nonspherical particles

like dust aerosols and ice crystals. Moreover, the considerable δ differences between spherical

fine particles and nonspherical coarse dust particles also enables the separation of dust extinction

from the total extinction profile retrieved by CALIOP (Yu et al., 2015; Song et al., 2021).

Formatted: Font: Cambria Math
Formatted: Font: 11 pt, Italic

Deleted: 2009). Moreover, the considerable δ

Deleted: δ is highly useful for aerosol and cloud classifications. First of all, if lidar backscattering is

dominated by single scattering, δ is close to zero for spherical or quasi-spherical particles like smoke aerosols and

water droplets. In contrast, δ is notably greater for nonspherical particles like dust aerosols and ice crystals.

Because of the fundamental importance of S and δ for lidar based dust remote sensing, previous

studies have made substantial effort to understand the connection between dust particle

properties, e.g., shape and size, and their lidar characteristics, in particular the S and δ (e.g.,

153 Dubovik et al., 2006; Gasteiger et al., 2011; Liu J. et al., 2015; Kahnert et al., 2020; Saito et al.,

2021; Saito and Yang, 2021; Kong, S. et al., 2022). The common methodology used in these

studies is to use light scattering models, such as the T-matrix (Mishchenko et al., 1996; Bi and

Yang, 2014b) and Discrete Dipole Approximation (DDA) model (Draine and Flatau, 1994, 2013;

Yurkin and Hoekstra, 2007, 2011), to compute the scattering properties including S and δ of dust

aerosols and then study the potential dependence on particle properties. Although these studies

have greatly improved our understanding and paved the foundation for the current aerosol

retrieval algorithms, they share a common limitation as they all used hypothetical dust particle

shape models, such as spheroid (Dubovik et al., 2006), irregular polyhedron (Saito et al., 2021),

Gaussian random sphere (Muinonen et al., 1996; Liu J. et al., 2015; Kahnert et al., 2020), tri-

Deleted: δ

Formatted: Font: Cambria Math

Deleted: δ

Formatted: Font: Cambria Math

Deleted: δ

Formatted: Font: Cambria Math

axial spheroids (Meng et al., 2010; Huang et al., 2023), and super-spheroid (Kong, S. et al., 2022) to simulate dust particle shapes that are weakly or not constrained by observations. The reason for this is probably two-fold. Most microscopic observations of dust particles in the literature are two-dimensional (2D) images based on scanning or transmission electron microscopes (SEM or TEM), while three-dimensional (3-D) observations are extremely rare. In addition, the implementation of complex shapes in scattering models is also a challenging task. For example, until recently the widely used T-matrix code based on the extended boundary condition method (Mishchenko et al., 1996) is primarily applicable only to rotationally symmetric particles such as spheroid. It is worth noting that the T-matrix method implementation based on the invariant imbedding T-matrix method is applicable to arbitrary shapes (Bi and Yang, 2014a). Aware of the limitation of hypothetical dust particle shape, these studies often use dust scattering properties from laboratory measurements as benchmark to select an optimal set of hypothetical shapes that <u>can</u> generate similar scattering properties, e.g., lidar characteristics, as measurements (Saito et al., 2021; Kong, S. et al., 2022). Nevertheless, the use of hypothetical instead of realistic dust shape inevitably leads to some important questions. Is the match of the dust scattering properties a result of a good shape model or a fortunate coincidence? If an optimal shape model is selected based on one set of dust scattering observations (e.g., δ at 532 nm), can this model automatically simulate other scattering properties (e.g., δ at other wavelengths)? Obviously, one way to address the above questions is to use realistic shape models in the computation of dust scattering properties. A few studies have made attempts in this direction. For example, Lindqvist et al. (2014) developed a so-called stereogrammetric surface retrieval method to construct 3-D dust shapes from 2D SEM dust images and Kemppinen et al. (2015 b) used a surface roughening model to add detail to the model. Ishimoto et al. (2010) and Kemppinen et al. (2015 a) used a

176

177

178

179180

181

182

183

184

185

186

187

188

189

190

191

192

193

194

195

196

197

198

Deleted: are able to

Deleted: δ

Deleted: δ

Deleted: along

Deleted:

Commented [8]: Just so you are aware, Ishimoto et al. (2010) tested the voronoi model for dust optics simulations earlier than Kemppinen.

Ishimoto, H., Zaizen, Y., Uchiyama, A., Masuda, K., & Mano, Y. (2010). Shape modeling of mineral dust particles for light-scattering calculations using the spatial Poisson–Voronoi tessellation. Journal of Quantitative Spectroscopy and Radiative Transfer, 111(16), 2434-2443.

Commented [9R8]: Thank you for this reference, I had not seen this paper previously

Voronoi tessellation-based algorithm to mimic dust internal structure. Järvinen et al. (2016) compared the lidar backscattering properties based on the constructed 3-D dust shapes with laboratory measurements and found reasonable agreements. An important finding from this study is that δ of realistic dust particles at 532 nm first increase with particle size but seems to approach an asymptotic constant value of \sim 0.30 for coarse dust particles.

Deleted: δ

Deleted: increases

The main objective of this study is to better understand the lidar backscattering properties of dust

particles with realistic shapes. The dust shape models used here are based on the focused ionbeam (FIB) tomography technique, aided by the energy dispersive X-ray spectroscopy (EDX)

and SEM imagining, developed by Conny et al. (2014) and Conny and Ortiz-Montalvo (2017),

which as far as we know is the most direct and faithful measurement of the shape and

morphology of single dust particles. In addition to shape measurement, the EDX is used to

measure the mineral composition of dust particles, which in turn enables the estimation of the

complex refractive index (CRI) of dust particles. Based on the measured dust particle shape and

estimated CRI, Conny et al. (2019, 2020) simulated and studied the scattering properties such as

single scattering albedo and phase functions of the dust samples using the DDASCAT model

220 (Draine and Flatau, 1994, 2013).

204

205

206

207

208

209

210

211

212

213

214

215

216

217

218

219

221

222

223

224

225

226

In this study, we focus on the lidar backscattering properties of realistic dust samples obtained

from FIB tomography measurements (Conny et al., 2019). For simplicity, we will refer to these

dust samples as "FIB dust samples." We are particularly interested in the following questions:

How do the S and δ of realistic dust samples vary with particle size, shape, mineral composition,

and lidar spectral channel? The remaining portion of the paper is organized as follows: First, in

Deleted: δ

Formatted: Font: Cambria Math

Section 2, we introduce the dust samples used in this study, along with their origins and properties. We also explain the Amsterdam Discrete Dipole Approximation (ADDA) model and introduce a convergence index to determine the number of orientations necessary for calculating the optical properties under the random orientation condition. In Section 3, we examine how the lidar backscattering properties of the dust samples depend on dust properties, including size, shape, and mineral composition. In Section 4, we present two dust δ parameterization schemes: one to estimate the δ of a single dust particle based on its size, and the other to estimate the δ of dust particles with a lognormal particle size distribution based on the effective radius. Finally, in Section 5, we summarize the main findings and conclusions of this study.

Deleted: δ

Deleted: δ

3. Data and model

3.1. FIB Dust Samples

The thirteen dust particles measured by FIB were obtained from the Mauna Loa Observatory (19° 32′ 10″N, 155° 34′ 34″W) on the island of Hawaii between March 15 and April 26, 2011. Six of these particles were collected during the daytime. Following Conny et al. (2019), these particles will be referred to as the "D" sample (e.g., "3D" indicates that the sample was collected during the daytime of day 3). The other eight particles were collected at night and are referred to as "N" samples. The properties of these particles, including their shape, size, and composition, as well as the measurement techniques, have been extensively documented in (Conny et al., 2019, 2020). Conny et al., (2019) analyzed the back trajectories from the Mauna Loa Observatory during this time interval, suggesting that their samples likely originated as Asian dust. Out of curiosity, we collocated the CALIOP observations with the back trajectories from the Hybrid Single-Particle Lagrangian Integrated Trajectory (HYSPLIT) model (Stein et al.,

Formatted: Outline numbered + Level: 1 + Numbering Style: 1, 2, 3, ... + Start at: 1 + Alignment: Right + Aligned at: 0.25" + Indent at: 0.5"

Formatted: Outline numbered + Level: 2 + Numbering Style: 1, 2, 3, ... + Start at: 1 + Alignment: Right + Aligned at: 0.75" + Indent at: 1"

Deleted: fourteen FIB

2015; Rolph et al., 2017) from March 25, 2011, 0000 UTC to March 18, 2011, 0000 UTC, starting from the Mauna Loa Observatory. The lidar depolarization ratio observations and aerosol classification (Figure 1c and e) results show large amounts of dust along the later portion of the projected path March 23rd, 2011. The back trajectories and CALIOP observations confirm that the FIB dust samples are likely long-range transported Asian dust particles, more specifically from the Gobi Desert, consistent with Conny et al. (2019). This may be an important distinction as Asian dust exhibits some differences in optical properties when compared to other regions such as the Sahara (Hofer et al., 2020; Floutsi et al., 2023), particularly in regards to the mineral composition discussion in Section 3.2 and 4.3. However, to our knowledge, there is no evidence to suggest that morphology of dust particles is strongly tied to regional origin. Therefore, while these dust particles are suspected to be of Gobi origin, we believe these dust samples to be useful for characterization of atmospheric dust more generally.

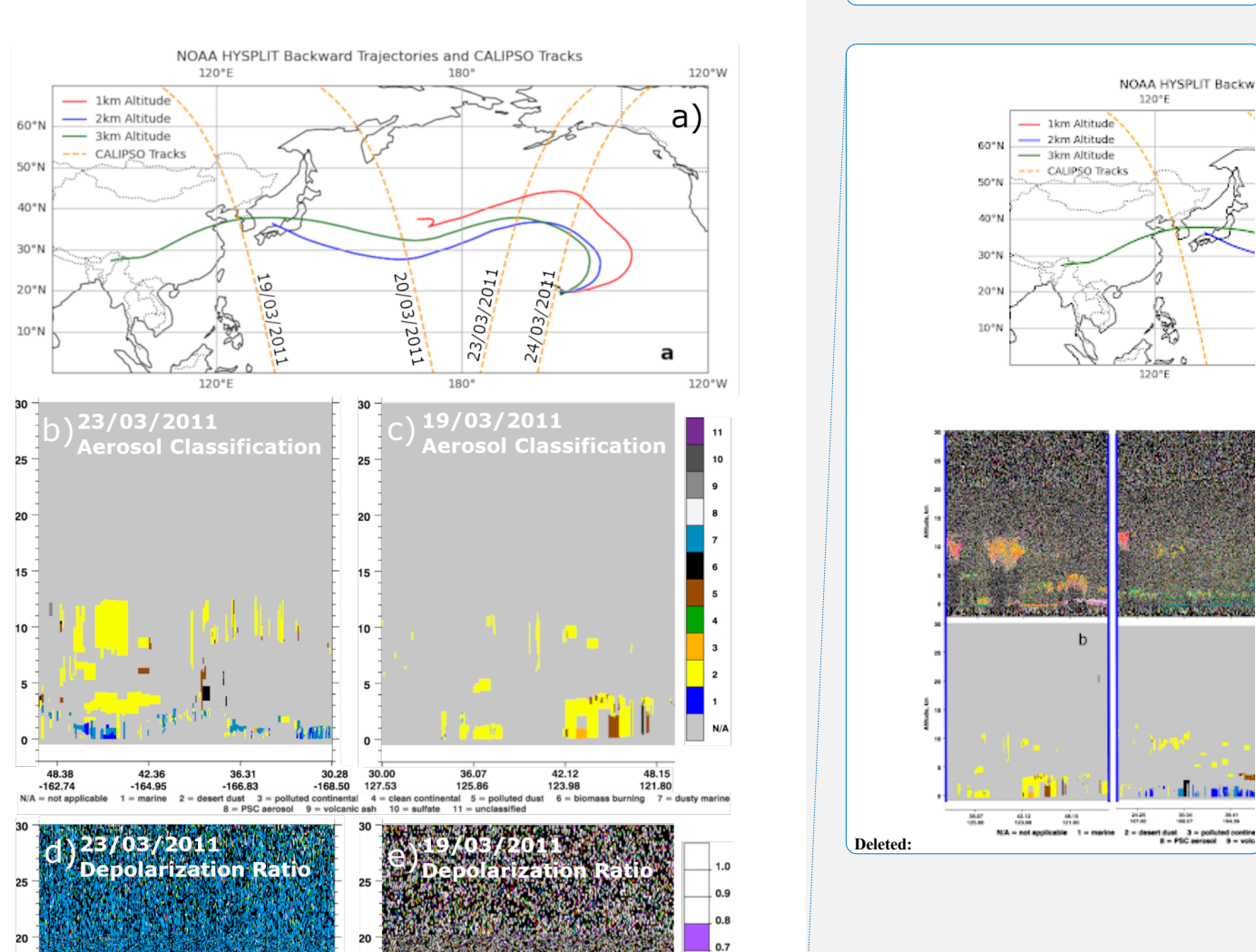
Deleted: 1d

Deleted: between

Deleted: 23 and March 24

Deleted: consistent with Conny et al. (2019).





42.36 -164.95 0.6

0.3 0.2 0.1

36.07 125.86 42.12 123.98 48.15 121.80

Formatted: Header 275 276 Figure 1. (a) NOAA HYSPLIT Backward Trajectory paths from March 25th, 2011 0000 UTC to March 18th, 2011 0000 UTC starting from Mauna Loa Observatory shown in solid lines. 277 278 North-South running dashed lines show CALIPSO tracks intersecting with the modeled dust Deleted: Vertical 279 paths. Depolarization ratio and aerosol subtype classification for CALIPSO tracks intersecting 280 with modeled dust paths from NOAA HYSPLIT Backward Trajectory for March 19th and 23rd, Deleted: , 20th, 281 2011 (b-e, respectively). Through δ and aerosol subtype classification, a dust plume was found Deleted: and 24th. Deleted: δ 282 to be present. In subplots b and c, yellow (labeled 2) corresponds with desert dust. 283 284 3.2. Dust particle shape and refractive index Formatted: Outline numbered + Level: 2 + Numbering Style: 1, 2, 3, ... + Start at: 1 + Alignment: Right + Aligned at: 0.75" + Indent at: 1" As emphasized above, the primary advantage of using FIB dust samples for this study is that the 285 286 shape and composition of these samples are directly measured. To determine the dust shape, the 287 FIB uses a gallium ion beam, milling through each particle in 15 nm to 20 nm increments. This 288 process results in a stack of 100 to 200 cross-sectional images with dimensions of 1024 by 884 289 pixels for each particle. These cross-sectional images are then combined to reconstruct highly 290 detailed 3-D dust shapes, composed of three-dimensional pixels or voxels as illustrated by an 291 example in Figure 2. 292 293 The collection of dust samples spans a range of sizes. In this study, we quantify this for irregular 294 geometries using the volume equivalent sphere radius (r_p) . Using this metric, our library covers Deleted:

a range from 0.46 μm to 0.93 μm in τυ. The particle geometries are also assigned two aspect

ratios, where orientation is determined through principal component analysis of the voxel

coordinates. This analysis aligns the longest axis along the z-direction and the greatest variation

295

296

297

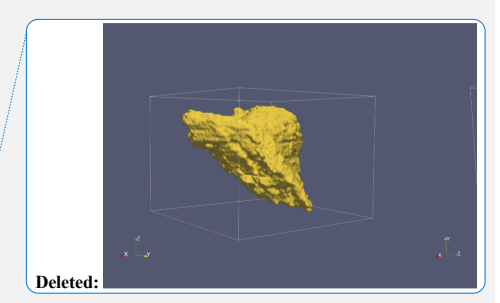
Deleted: volume equivalent radius (r_v) .

from this axis with the *x*- and *y*-directions, aligning with an intuitive understanding of defining aspect ratios in three dimensions. The aspect ratios of these particles vary from 0.629 and 0.398 (particle 2N Ca-S) to more symmetrical particles with aspect ratios of 0.582 and 0.575 (particle 4N1 CaMg).



Figure 2. Orthographic projection of a sample dust particle from the FIB reconstructed database, 3D Ca-Rich.

In addition to the FIB-based dust shape reconstruction, Conny et al. (2019) also performed the element composition and mineral phase analysis for the FIB dust samples using the SEM and energy-dispersive X-ray spectroscopy (EDX). They found that the dust samples can be loosely classified into three categories based on the element compositions, the mainly Calcium Magnesium based (Ca-Mg), the Calcium rich (Ca-rich) ones and lastly those primarily composed of Calcium Sulfide (Ca-S). In this study we follow this naming convention of Conny et al., 2019. To determine the refractive index of the dust samples, Conny et al. (2019) first estimated the volume fractions of possible mineral phases in the particles based on the composition analysis results. Then, the complex refractive index of each particle was determined through the average Maxwell-Garnett dielectric function based on the estimated volume fraction of each mineral



Commented [10]: This 3D (Day 3 sample) is very easy to be confused with 3-D (3-dimentional). You may consider changing 3D to other symbol, e.g., D3.

Deleted: We shall

Deleted: their classification and

Deleted: in this study (see

Deleted:).

Deleted: has

Deleted: index

phase. It should be noted that the iron-phase composition in the particle was assumed to be either siderite, hematite, or magnetite which have different complex refractive indices. Moreover, two sets of complex refractive index were used for each iron-phase mineral to account for the variability induced by optical anisotropy. The combination of mineral differences and refractive index variability lead to several sets of final refractive index after the Maxwell-Garnett average. Take the 3D Ca-Rich particle in Figure 2 for example. Table 1 provides the complex refractive indices at 589 nm from Conny et al. (2019) for a single particle. Interested readers are referred to their study for more information.

Deleted: possible

Deleted: index

Deleted:).

Table 1. The possible complex refractive index at 589 nm of the 3D Ca-Rich particle in Figure 2 from Conny et al. (2019).

Iron-phase	Minimum	Minimum	Maximum	Maximum	
mineral	Refractive Index	ractive Index Refractive Index Refractive Inde		Refractive Index	
	Real	Imaginary	Real	Imaginary	
Magnetite	1.532	2.14E-02	1.660	2.36E-02	
Hematite	1.544	2.32E-03	1.681	2.28E-03	
Siderite	1.508	1.34E-05	1.648	1.34E-05	

Formatted Table

In this study, we are interested in the dust scattering properties at three commonly encountered lidar wavelengths, namely, 355 nm, 532 nm, and 1064 nm. For simplicity, we assume the same refractive index from Conny et al. (2019) for all three wavelengths, which is probably reasonable only for the 532 nm. On the other hand, because we assume the refractive index to be invariant with wavelength, the wavelength variation essentially corresponds to the variation of dust

particle size parameter $x = 2\pi r/\lambda$, allowing us to focus on the impact of dust particle size on the lidar scattering properties. The impacts of the spectral variation of refractive index will be investigated in future studies.

Deleted: the

354

355

356

357

358

359

360

361

362

363

364

365

366

367

368

369

370

371

372

350

351

352

353

3.3. ADDA model and convergence index of random orientation.

In this study, we utilize the ADDA model version 1.4.0 to compute the single scattering properties, including the extinction cross section \mathcal{L}_{ext} , single scattering albedo ω , and scattering matrix P, of each FIB dust particle. The scattering properties of dust particles depend on not only their size, shape, and refractive index, but also their orientations with respect to the incident light, and the wavelength of incident light. In this study we assume that dust particles are randomly oriented. The theoretical basis and numerical implementation of the ADDA model have been well documented (Yurkin and Hoekstra, 2007, 2011). It has been used in numerous previous studies to compute the scattering properties of aerosol and cloud particles (Yang et al, 2013; Gasteiger, 2011; Collier et al, 2016). The process to generate the inputs from the FIB shape measurements for the discrete dipole approximation (DDA) model has been described in detail in Conny et al. (2019). We use the same inputs and configurations in this study. The only difference is that we use the ADDA model while Conny et al. (2019) used a different DDA model, DDSCAT, by Draine and Flatau (1994). The reason we cannot directly use the DDA simulation results from Conny et al. (2019) is twofold. Firstly, their computations are conducted for an incident light at the 589 nm wavelength, whereas we are interested in lidar wavelengths of 355 nm, 532 nm, and 1064 nm. Secondly, as will be explained later, we will need a greater number of orientations to simulate random orientation for P and lidar backscattering properties Formatted: Outline numbered + Level: 2 + Numbering Style: 1, 2, 3, ... + Start at: 1 + Alignment: Right + Aligned at: 0.75" + Indent at: 1"

Commented [711]: you have explained this before

Deleted: σ_e

Deleted: ω

Deleted: phase

Deleted: P

Deleted:

Deleted: P

(Konoshonkin et al., 2020) than may be sufficient for the φ_e and ω to converge. In the remainder of this section, we will introduce a practical method to determine if a sufficient number of orientations have been used in the ADDA simulations to ensure convergence in the results for random orientation computations.

Deleted: $σ_e$ Deleted: ω

For a particle with an irregular shape and arbitrary orientation, the scattering matrix P that relates the incident and scattering Stokes parameters is a 4x4 matrix with 16 elements

Deleted: phase

Deleted: P

 $P = [P_{11}(\theta_s) P_{12}(\theta_s) P_{13}(\theta_s) P_{14}(\theta_s) P_{21}(\theta_s) P_{22}(\theta_s) P_{23}(\theta_s) P_{24}(\theta_s) P_{31}(\theta_s) P_{32}(\theta_s) P_{32}(\theta_s)]$

 $\begin{array}{|c|c|c|c|c|c|} \hline & r^{P_{11}(\theta_s)} & P_{12}(\theta_s) & P_{13}(\theta_s) & P_{14}(\theta_s) \\ \hline \textbf{Deleted:} & P_{21}(\theta_s) & P_{22}(\theta_s) & P_{23}(\theta_s) & P_{24}(\theta_s) \\ \hline & P_{31}(\theta_s) & P_{32}(\theta_s) & P_{33}(\theta_s) & P_{34}(\theta_s) \\ \hline & P_{41}(\theta_s) & P_{42}(\theta_s) & P_{43}(\theta_s) & P_{44}(\theta_s) \\ \hline \end{array}$

Formatted Table

Commented [12]: The equation does not look like a 4x4 matrix but a function of 16 elements. Probably, my version of Microsoft Word is not working properly.

Commented [13R12]: Yes equation issues like this happen for me as well when going between google and microsoft. I add all changes to a word document as well.

Deleted: θ_s

Deleted: phase

where θ_s is the scattering angle. If the particle is randomly oriented, for any orientation its reciprocal orientation is equally likely. Because of the reciprocal symmetry, the scattering matrix for randomly oriented particle with irregular shape reduces to (van de Hulst 1957; Mishchenko et al., 2002; Mishchenko and Yurkin, 2017)

•

 $[P_{11}(\theta_s) P_{12}(\theta_s) P_{13}(\theta_s) P_{14}(\theta_s) P_{12}(\theta_s) P_{22}(\theta_s) P_{23}(\theta_s) P_{24}(\theta_s) - P_{13}(\theta_s) - P_{13}(\theta_s) P_{24}(\theta_s) P_{24}(\theta_s)$

The symmetry property of the *P* matrix for randomly oriented particles in Eq. (5) provides a

basis to assess the convergence of random orientation simulations in ADDA. For example,

utilizing the fact that $P_{41} = P_{14}$ for <u>a</u> randomly oriented <u>particle</u> we can define a convergence

index (CI) for random orientation as

380

381

382

383

384

385

386

387

388

389

390

391

392

393

394

395

396

Deleted: P

Formatted Table

Deleted: particles

407

408

409

410

411

412

 $CI = \int_0^{\pi} (P_{14}(\theta_s) - P_{41}(\theta_s))^2 d\cos(\theta_s)$

As such, CI approaches zero when the random orientation computation converges. It should be

such as $P_{21} = P_{12}$, $P_{31} = -P_{13}$. For practical applications, we usually assume that particles are

randomly oriented with an equal number of mirror particles. Under such a condition, or if the

particle in question has mirror symmetry itself, the scattering matrix has only 6 independent

elements in the form (van de Hulst 1957; Mishchenko and Yurkin, 2017; Yang et al., 2023):

noted that CI can also be defined based on other symmetric elements of the scattering matrix

(6)

Commented [14]: did you miss 1/2 before the integral?

Deleted: $CI = \int_0^{\pi} (P_{14}(\theta_s) - P_{41}(\theta_s))^2 d \cos(\theta_s)$.

 $P_{22}(\theta_s)$

0

 $P_{33}(\theta_s)$ $P_{34}(\theta_s)$

Formatted Table

Formatted: Header

Deleted: that

Deleted: phase

Deleted: phase

413 414

 $[P_{11}(\theta_s) P_{12}(\theta_s) 0 0 P_{12}(\theta_s) P_{22}(\theta_s) 0 0 0 0 P_{33}(\theta_s) P_{34}(\theta_s) 0 0 - P_{34}(\theta_s) P_{44}(\theta_s) (7)]$

Deleted: $P_{12}(\theta_s)$

Formatted Table

and a CI based on $P_{12} = P_{21}$ or $P_{34} = -P_{43}$ must be used.

416

415

417 In the context of ADDA, the orientation of a particle with respect to the incidence is defined by 418

419

420 421

422

423 424

using three Euler angles α , β , and γ . To specify a certain orientation, the particle is rotated first α on the z-axis, then β on the y-axis, and finally γ across the new z-axis through the zyz convention (Yurkin and Hoekstra, 2020). Then, to produce the scattering properties for a randomly oriented particle, ADDA averages across a large number of orientations. ADDA can do this internally through specified number of evenly spaced intervals across α , β , and γ . For α and β , ADDA calculates the scattering properties for the new orientation while for γ , or the selfrotation angle, it equivalently rotates the scattering plane to improve computational time. It Deleted: α, β

Deleted: y

Deleted: a

Deleted: β

Deleted: y

Deleted: y

Formatted: Font: 11 pt

calculates orientations in intervals of $2^n + 1$ for each of α , β , and γ resulting in $\{(2)^n + 1)^3$ total orientations. To assess if the random orientation convergence has been achieved, one can examine the behavior of CI as well as other scattering properties of interest, as a function of the number of orientations. An example using the 3D Ca-Rich dust particle is shown in Figure 3 for n = 1, 2, ..., 6. As expected, all properties converge to asymptotic values as n increases from n = 1 (i.e., 27 orientations) to n = 1 (i.e., 274,625 orientations). On the other hand, it is important to note that the scalar properties such as extinction efficiency and asymmetry factor (Figure 3a), and β and β (Figure 3b) have converged when n = 1, while the N based on certain scattering matrix elements (Figure 3c) only converged after n = 1. Based on this result, we employ n = 1 for the computations in this study. The results in Figure 3 clearly show that although one can assess the convergence of random orientation computation by observing the asymptotic behavior of scalar properties, the N based on scattering matrix elements is a more robust index supported by fundamental physics.

436

437

438

439

440

441

442

443

444

445

446

447

448

449

450

451

452

453

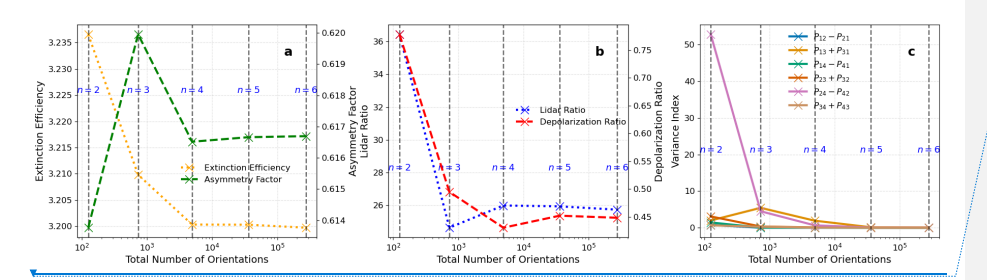


Figure 3. (a) Change in extinction efficiency and asymmetry factor with increasing <u>number of</u> orientations for a representation of a randomly oriented <u>dust</u> particle <u>3D Ca-Rich</u>. (b) <u>S</u> and <u>linear depolarization ratio</u> as <u>function of</u> the number of orientations <u>for dust particle 3D Ca-</u>

Formatted: Header

Deleted: $(2^n + 1)^3$

Formatted: Font: Cambria Math

Formatted: Font: Cambria Math

Formatted: Font: 11 pt

Formatted: Font: 11 pt

Formatted: Font: 11 pt

Deleted: ,...,

Formatted: Font: Cambria Math

Formatted: Font: Cambria Math

Formatted: Font: Cambria Math

Formatted: Font: Cambria Math

Deleted: 8

Formatted: Font: Cambria Math

Deleted: 262,144

Deleted: δ

Deleted: phase

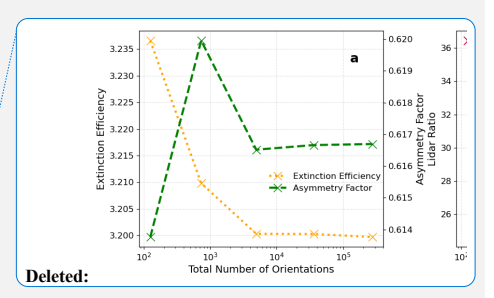
Formatted: Font: Cambria Math

Formatted: Font: Cambria Math

Formatted: Font: Cambria Math

Formatted: Font: Cambria Math

Deleted: phase



Deleted: single-scattering albedo

Deleted: The

Formatted: Font: Cambria Math

Deleted: ratio's convergence

Deleted: used increases.

	→		Formatted: Header
466	Rich. (c) Convergence Index for each of dust particle 3D Ca-Rich's Mueller index pairs at 532		Commented [15]: The label in Fig 3c shows "variance Index". This should be "Convergence Index".
467	nm. Note figures start at $n = 2$.		Deleted: n
l 468			
469	Thus, the error in computations of optical properties through ADDA is strongly tied to the		
470	number of orientations used. We find in section 3 constraining refractive index through		
471	mineralogy and size through proper characterization of particle size distribution are the largest		
472	potential sources of error in these calculations, as ADDA's integration error has been set to less		
473	than 10 ⁻⁵ and the geometries used are highly detailed, with individual dipole sizes on the order		
474	of $\frac{10^3}{10^3}$ nm ³ . This makes the numerical error negligible compared to the error in chosen		Deleted: ~20
l 475	parameters, convergence level, and sample size through the limited set of geometries. The CI is		
476	a tool to minimize computational error while considering computational cost.		
477			
478	With the help of the newly developed CI, we computed the scattering properties of the FIB dust		
479	samples for three commonly encountered lidar wavelengths 355 nm, 532 nm, and 1064 nm. For		
480	each wavelength, more than 60 ADDA simulations are carried out corresponding to different		
481	particles, as well as different refractive indices for each particle as explained above (see section		
482	2.2). Figure 4 shows the <u>scattering</u> matrix elements P_{11} and P_{22}/P_{11} for the FIB dust samples for		Deleted: phase
483	the three lidar wavelengths, for their minimum refractive index for each mineral typing. Given		Deleted: .
484	the realistic morphology of the FIB dust samples and extensive computational methods of		
485	determining these optical properties, the FIB dust samples can serve as a benchmark for future		Deleted: shown in Figure 4
486	studies on <u>simulated</u> mineral dust scattering properties. As one can see in Figure 4 a-c, the values		
487	of P_{11} in the forward scattering directions <u>increase</u> systematically from 1064 nm to 532 nm, and	************	Deleted: increases
488	355 nm, which can be explained by the increase of size parameter as wavelength decreases. In		Deleted: $x = \pi D/\lambda$

Figure 4 d-f, $P_{22}(\pi)/P_{11}(\pi)$ shows considerable decreases from 1064 nm to 532 nm, down ~13% on average. In contrast, the changes are relatively small from 532 nm to 355 nm. These features will help us understand the spectral dependence of S and S shown and discussed in the

Deleted: δ

Deleted: the

Formatted: Font: Cambria Math

next section.

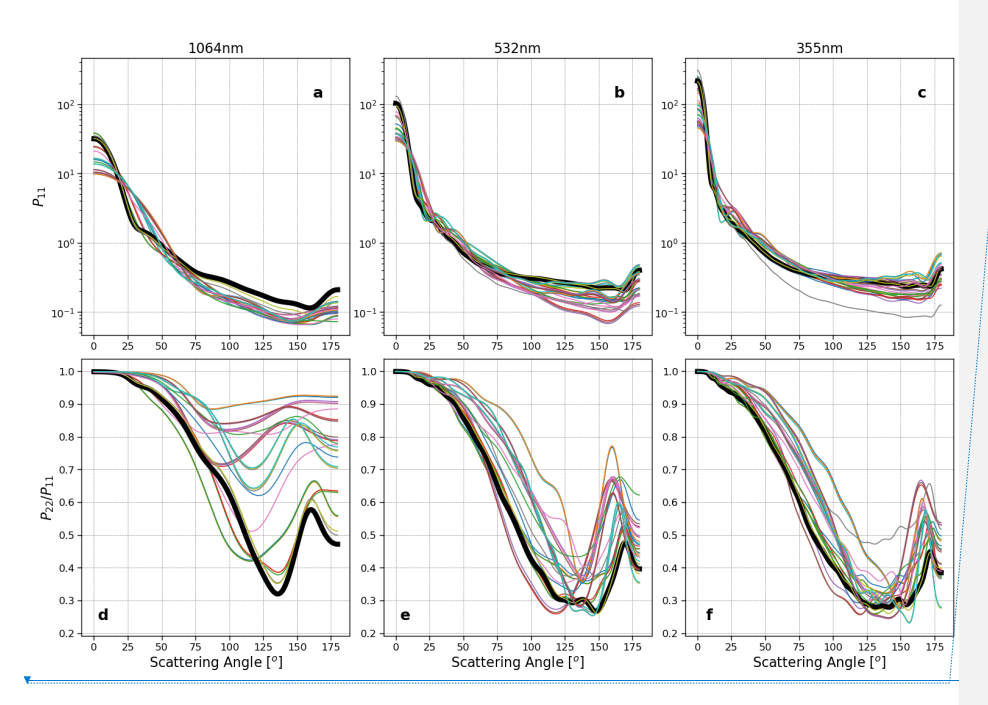
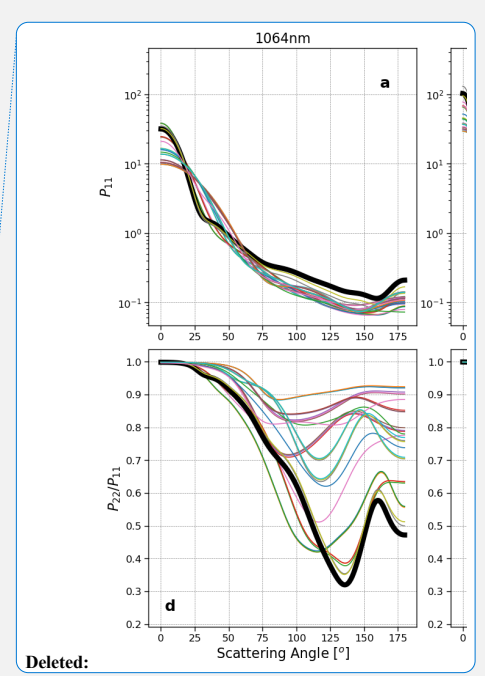


Figure 4. P_{11} and P_{22}/P_{11} for each particle geometry. Results for (a, d) 355 nm, (b, e) 532 nm, (c, f) 1064 nm of each iron-containing mineral phase's minimum refractive index. Highlighted in black is particle 3D Ca-Rich.



4. Sensitivities of lidar ratio and depolarization ratio to particle properties

4.1. Sensitivity to dust particle <u>size</u>

510

511

512

513

514

515

516

517

518

519

520

521

522

523

In lidar-based aerosol remote sensing, the S - S diagram is often used to classify aerosols into different types (Burton et al., 2012; Illingworth et al., 2015). The S - S diagram for the FIB dust samples is shown in Figure 5. Notably, S is negatively correlated with S when the results for all three wavelengths are combined (correlation coefficient of 0.83). Specifically, the S at 1064 nm is smaller than the corresponding values at 532 nm and 355 nm, while the opposite is true for the S. The results for 532 nm and 355 nm largely overlap with each other. Recall that the same CRI is used for all three wavelengths, so these spectral differences are caused by the size parameter difference, i.e., the relative size of the particle with respect to the lidar wavelength. To further illustrate this point, we plotted the S and S separately as a function of the dust particle size parameter, shown in Figure 6. Note that the size of the irregular particle can be defined in different ways; here, we adopt the volume-equivalent size.

Formatted: Outline numbered + Level: 1 + Numbering Style: 1, 2, 3, ... + Start at: 1 + Alignment: Right + Aligned at: 0.25" + Indent at: 0.5"

Deleted: sizes

Formatted: Header

Formatted: Outline numbered + Level: 2 + Numbering Style: 1, 2, 3, ... + Start at: 1 + Alignment: Right + Aligned at: 0.75" + Indent at: 1"

Deleted:

Formatted: Font: Cambria Math

Formatted: Font: Times New Roman

Deleted: δ

Formatted: Font: Cambria Math

Formatted: Font: Times New Roman

Deleted: δ

Formatted: Font: Cambria Math

Deleted: δ

Formatted: Font: Cambria Math

Deleted: δ

Formatted: Font: Cambria Math



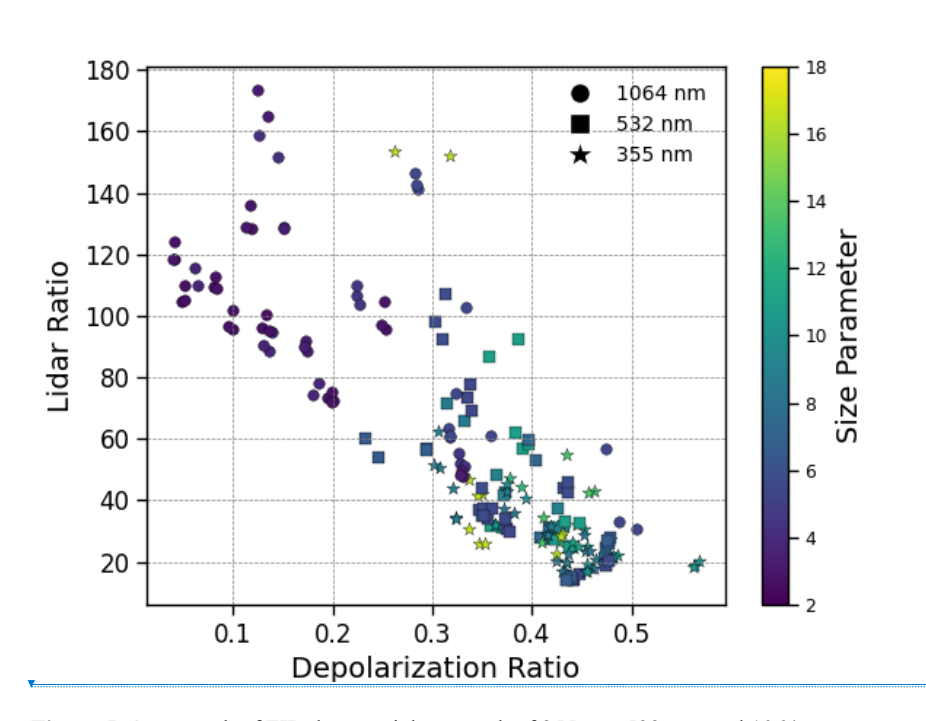
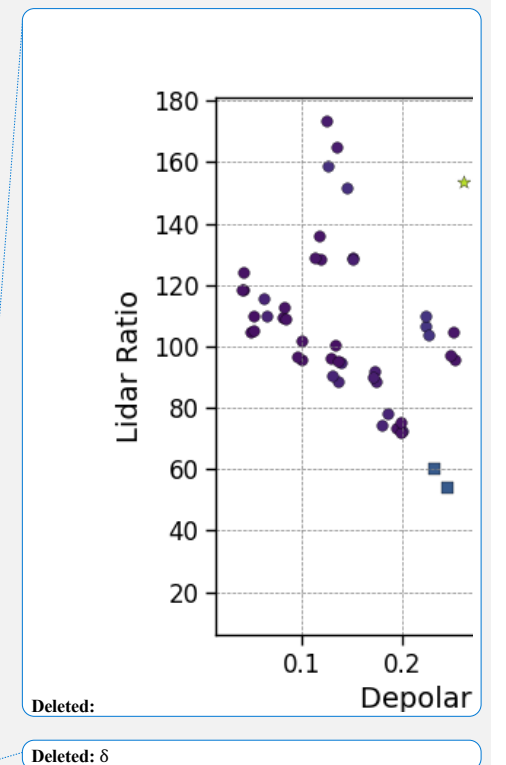


Figure 5. $S \rightarrow \delta$ graph of FIB dust particles at each of 355 nm, 532 nm, and 1064 nm wavelengths for the refractive index of each mineral type found present in the particle.

Figure 6 reveals an interesting asymptotic behavior of lidar properties with respect to size, where S (Figure 6a) and S (Figure 6b) first decreases and increases, respectively, with size parameters and then seemingly approach their asymptotic values. We use a locally weighted scatterplot smoothing regression (or LOWESS) to fit the trend in lidar optical properties with size parameters. We find that both S and S plateau around size parameter S and then approach to their asymptotic values, $S = 35 \, sr$ and S and S and S and S and S and S are essent in the dust particles analyzed and



Formatted: Font: Cambria Math
Formatted: Font: Times New Roman

Deleted: δ
Formatted: Font: Cambria Math

 Deleted: δ

 Formatted: Font: Cambria Math

 Formatted: Font: (Default) Gungsuh

 Deleted: $35sr^{-1}$

 Deleted: δ

 Deleted: . The

the computational expense to produce simulations of larger particles. However, the asymptotic behavior of lidar properties $\underline{\text{has}}$ also been reported in several previous studies. For example, the S and S based on the so-called super-spheroid dust model in Kong, S. et al. (2022) showed a similar asymptotic behavior for the size parameter range between 2 and 20 (see their Figure 3), and so is the laboratory measured dust S in Järvinen et al. (2016) (see their Figure 9).

548

549

550

551

552

553

554

555

556

557

558

559

560

561

562

563

Deleted: have

Deleted: δ

Formatted: Font: Cambria Math

idar Ratio

Deleted: δ

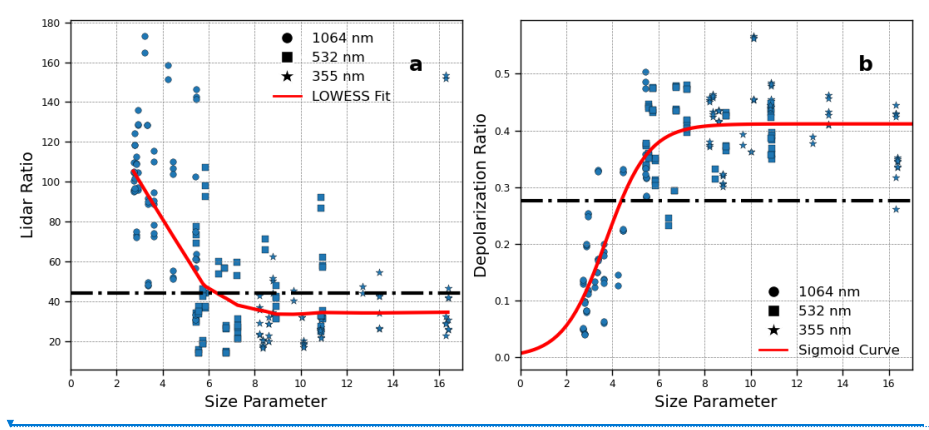
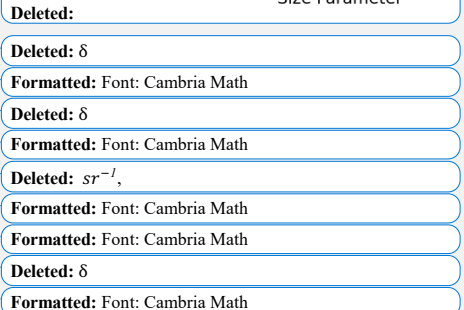


Figure 6. Relationship between dust particle size parameter and (a) S and (b) S. The red line is a LOWESS fit of the data for S and a Sigmoid function for S. The black lines correspond to (a) S = 44, Sr, the S used for CALIPSO's aerosol classification of dust (Kim et al., 2018) and (b) S = 0.277, the median observed S at 532 nm of the Atlantic dust transport region using CALIOP (Liu S. et al., 2015).



1064 nm

532 nm

355 nm

LOWESS

Size Parameter

Since S is a function of both $P_{11}(\pi)$ and the ω , we investigate their relative roles in determining the size dependence of S. Figure 7a shows that the values of S lie closely around the $1/P_{11}(\pi)$ line, with the r-square value around 0.97 for a simple regression of $S = 12.9/P_{11}(\pi)$. In contrast,

Deleted: (π)

Deleted: ω

Formatted: Font: Cambria Math

Deleted: (π)

Formatted: Font: Cambria Math

Formatted: Font: Cambria Math

Deleted: (π)

single-scattering albedo ω plays a lesser role in S among the particles tested due to greater similarities in values (Figure 7b). However, the outliers in Figure 7a correspond to points with much lesser ω in Figure 7b, particularly the FIB sample 3D Ca-rich (see Figure 2) using the magnetite refractive index, which has an imaginary refractive index of 0.021 to 0.024, an outlier with a magnitude ten times greater than the other mineral types present (See Table 1). In Figure 7c and d, we plot the variation of $P_{11}(\pi)$ and ω respectively as a function of size parameter. Although the variability of $P_{11}(\pi)$ is quite large, especially in the size parameter range between 5 and 10, it generally increases with size parameter. In contrast, the ω in Figure 7b shows a slight decrease with size. These results indicate that $P_{11}(\pi)$ plays a more dominant role than the ω in determining the size dependence of S in these dust samples.

576

577

578

579

580

581

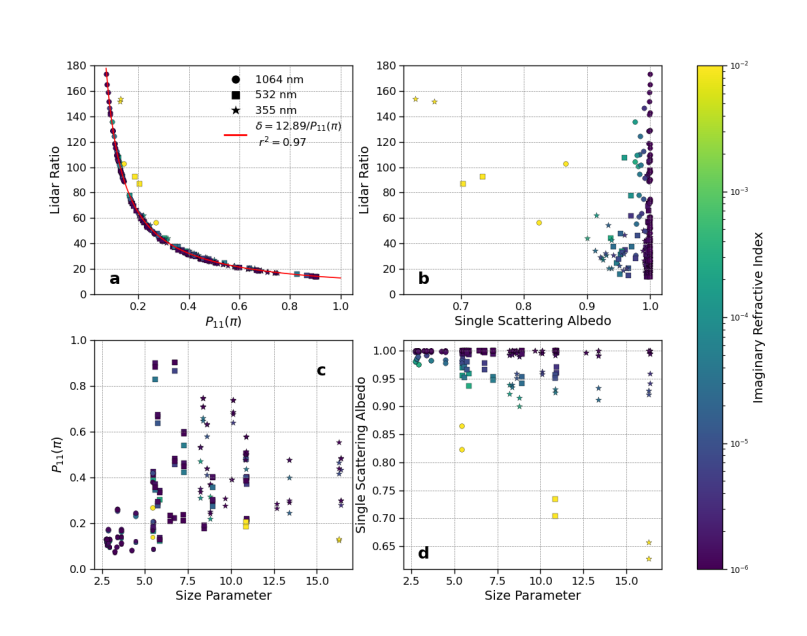
582

583

584

585

586



Formatted: Header

Deleted: ω

Formatted: Font: Cambria Math

Deleted: ω

Deleted: (π)

Deleted: ω

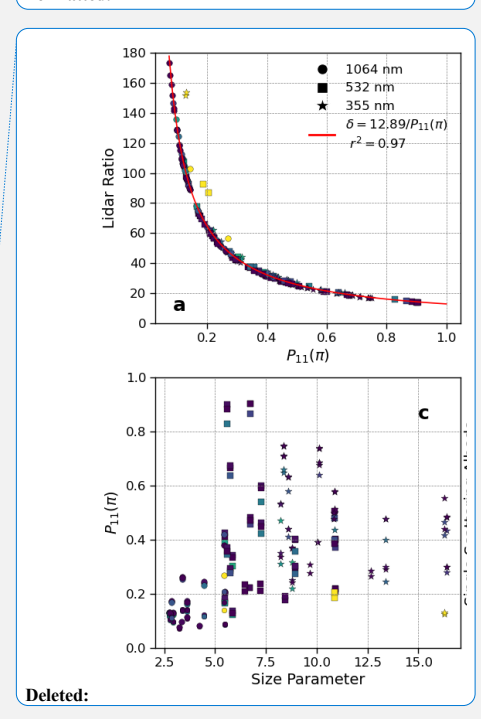
Deleted: (π)

Deleted: ω

Deleted: (π)

Deleted: ω

Formatted: Font: Cambria Math



Deleted: ω
Deleted:

Figure 7. S as a function of a) P_{11} and b) ω . c) P_{11} and d) ω as a function of dust size parameter. The color of each dot corresponds to the imaginary refractive index.

598

599

600

601

602

603

604

605

606

607

608

609

610

611

612

613

614

596

597

Following the same thought for the above S analysis, we analyze the role of $P_{11}(\pi)$ and $P_{22}(\pi)$ in determining the asymptotic behavior of S in Figure 6b. It is seen in Figure 8a and b that both $P_{11}(\pi)$ and $P_{22}(\pi)$ increase with dust size. Interestingly, their ratio $P_{22}(\pi)/P_{11}(\pi)$ first decreases with size and then seems to approach an asymptotic value of 0.4 when dust particles are large. So, the result suggests that the asymptotic trend of S with respect to dust size is a result of the asymptotic behavior of $P_{22}(\pi)/P_{11}(\pi)$.

Deleted: ω Formatted: Font: Cambria Math

Deleted: $x_v = 2\pi r_v/\lambda$.

Deleted: of the imaginary

Deleted: (π) Deleted: (π) Formatted: Font: Cambria Math

Deleted: δ Deleted: (π) Deleted: (π) Deleted: (π) Deleted: (π)

Deleted: (π) Deleted: δ

Deleted: (π) Deleted: π

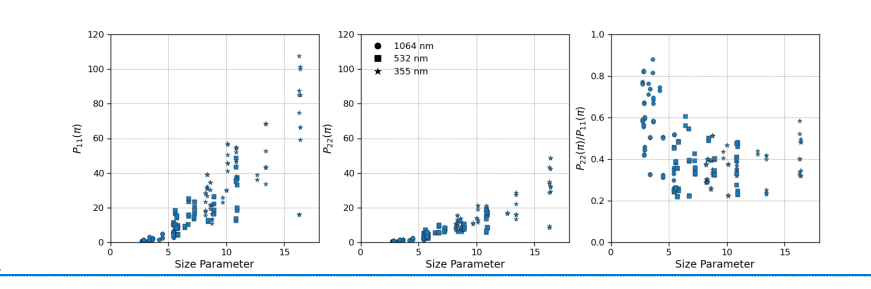
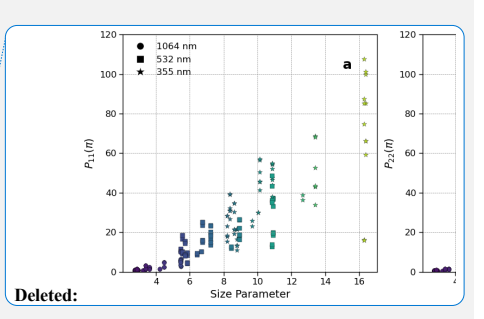


Figure 8. a) $P_{11}(\pi)$, b) $P_{22}(\pi)$ and c) $P_{22}(\pi)/P_{11}(\pi)$ as a function of the dust particle size parameter.



Deleted: (π) ,
Deleted: (π)

Deleted: (π)

4.2. Sensitivity to dust shape and sphericity

Several studies have shown that constraining particle morphology is important for quantifying the δ of dust particles (Dubovik et al., 2006; Saito et al., 2021; Liu J. et al., 2015; Kahnert et al., 2020; Kong, S. et al., 2022). As explained in the introduction, most of these studies are based on

Formatted: Outline numbered + Level: 2 + Numbering Style: 1, 2, 3, ... + Start at: 1 + Alignment: Right + Aligned at: 0.75" + Indent at: 1"

Deleted: δ

simple hypothetical shape models such as ellipsoid and irregular hexahedrons. In this section, we investigate the dependence of δ on dust sphericity based on the FIB dust samples. As explained in section 2.2, in the baseline simulations each dust sample has different sizes and CRI that corresponds to laboratory measured dust mineralogy. As a result, the differences in δ between different sample particles in the baseline simulations are caused by not only shape but also size and CRI differences. To eliminate the influence of size and CRI and focus on the effect of sphericity, we carried out an additional set of ADDA computations for the 532 nm wavelength, where we used the same CRI of n = 1.5 + 0.005i and the same volume-equivalent radius of 0.5 μ m for all the FIB particles but kept the original shape of each particle. The use of the common size and CRI allows us to investigate the dependence of δ on the sphericity index defined as follows (Wadell, 1935; Saito and Yang, 2022):

Deleted: δ

Deleted: session

Formatted: Header

Deleted: δ

Formatted: Font: Cambria Math

Deleted: δ

Formatted: Font: Times New Roman

 $\Psi = \frac{\pi^{1/3} (6V)^{2/3}}{A_s},$ (8)

Deleted: $\Psi = \frac{\pi^{1/3} (6V)^{2/3}}{A_s}$

Formatted Table

Deleted: Ψ

Deleted: Ψ

Deleted: δ

Deleted: Ψ

Deleted: the

Where Ψ is the sphericity, V is the volume of the particle, and A_s is the surface area. By

definition, a sphere is Ψ =1, and a perfectly spherical particle has a δ of 0. However, due to the

irregularity of the FIB dust sample geometries, their \(\mu \), more specifically the surface area, is

heavily impacted by the level of granularity in voxel size, similar to the well-known coastline

paradox (Steinhaus, 1954). Therefore, we employ the effective sphericity as the average

projected area of a particle is not susceptible to the same issues of increasing value with precision

653 (Vouk, 1948; Saito and Yang, 2022):

635

636

637

638

639 640

641

642

643

644

645 646

647

648

649

650

651

652

 $\Psi_{eff} = \frac{\pi^{1/3} (6V)^{2/3}}{4A_{proj}},$

Deleted: $\Psi_{eff} = \frac{\pi^{1/3} (6V)^{2/3}}{4A_{proi}},$

Formatted Table

(9)

665

666

667

668

669

670

671

672

673

674

675

676

677

678

679

particle size.

Where ψ_{eff} is the effective sphericity and A_{proj} is the average projected area across all projection directions. This gives us a wide range of effective sphericity between 0.49-0.89. As shown in Figure 9, we find no clear relationship between effective sphericity and δ or δ (null hypothesis rejected with $\rho > 0.05$ for both δ and δ). This may be a result of a limited set of geometries of the FIB dust samples. It could also be due to the limitation of the effective sphericity index in Eq. (9) failing to capture the subtle dependence of δ on dust particle shape. Note that other previous studies have also found weak dependence of δ in particle sphericity (e.g., Saito and Yang, 2021; Kong, S. et al., 2022). Further studies are warranted to better understand the relationship between the δ and morphology of dust particles. But overall, our results seem to suggest that the impact of particle sphericity on δ and δ is less important than

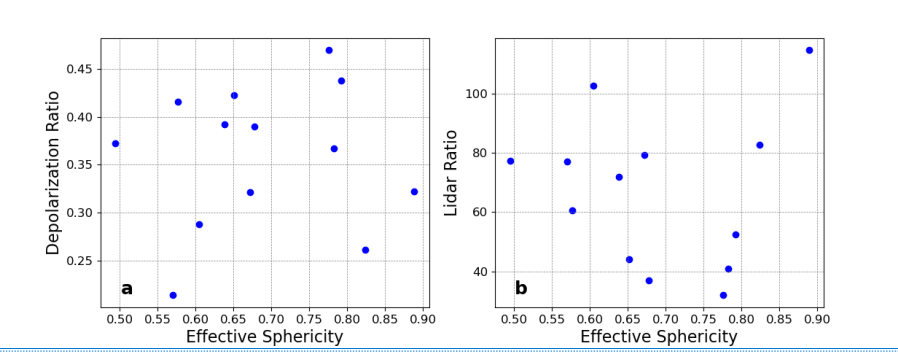


Figure 9. (a) Effective sphericity dependence of δ . (b) Lidar ratio variance with effective sphericity. A common volume is used by constraining the volume equivalent sphere radius to

Deleted: Ψ_{eff}

Deleted: δ

Formatted: Font: Cambria Math

Deleted: δ

Formatted: Font: Cambria Math

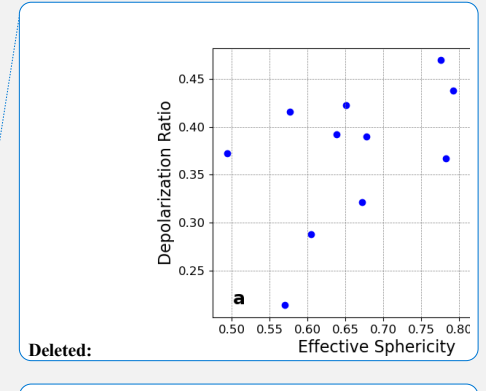
Deleted: δ

Deleted: δ

Deleted: δ

Deleted: δ

Formatted: Font: Cambria Math



Deleted: δ

0.5 μ m for each particle as well as a refractive index of $n_v = 1.5 + .005i$. A wavelength of 532 nm was used.

Deleted: =

Formatted: Font: Cambria Math

4.3. Sensitivity to dust mineralogy

Each particle from Conny et al.'s study (2019) was determined to have different amounts of iron in its composition through their EDX spectroscopy tests. Using this data, they determined the refractive index of each particle with the Maxwell-Garnett dielectric function described in section 2.3. The tests resulted in the percentage of elements by mass and volume, but did not reveal the mineral phase within the dust. To account for this, the study uses various possible iron containing mineral phases for each particle to determine the refractive index, as these phases have the greatest variability in possible refractive index for these particles. They also account for birefringence through a minimum and maximum value for refractive index. Each particle was given a hematite phase, while some had magnetite, ankerite, and/or siderite present. Interested readers are directed to Conny et al. 2019 for further details.

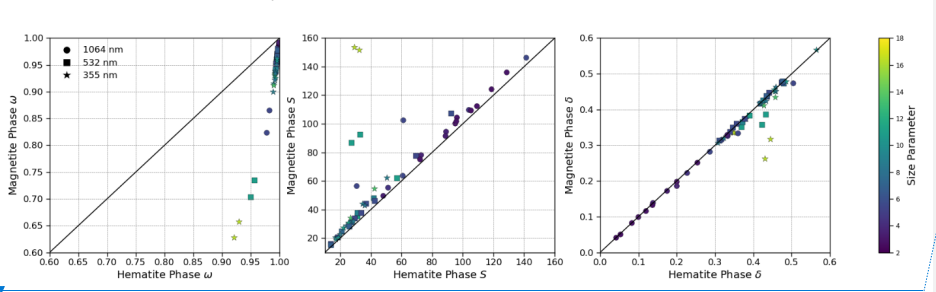
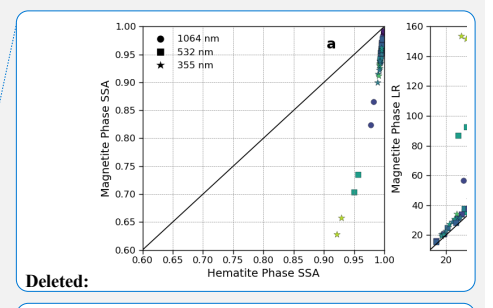


Figure 10. Variation of a) ω , b) S, and c) δ for each particle with its magnetite phase and corresponding hematite phase.

Formatted: Outline numbered + Level: 2 + Numbering Style: 1, 2, 3, ... + Start at: 1 + Alignment: Right + Aligned at: 0.75" + Indent at: 1"



Deleted: ω

Deleted: δ

Formatted: Font: Cambria Math

Formatted: Header Each of these mineral phases has a different CRI, with magnetite being the most absorbing of 712 713 the iron-containing phases present (see Table 1). This results in considerable variations (up to 714 32%) in single scattering albedo (Figure 10a), particularly for the 3D Ca-Rich particle, which Deleted: particles 715 has the highest iron content by mass, ranging from 11.4 % to 7.90 % depending on the mineral Deleted: have Deleted: %. phase used. In contrast, the next most iron-dense particle (4N1 Ca-Mg) contains only 4.35 % to 716 717 1.56 %. Accompanying the reduction in single scattering albedo, the S becomes systematically Formatted: Font: Cambria Math 718 larger (Figure 10b), and the 5 becomes smaller (Figure 10c) when hematite is replaced by Deleted: δ 719 magnetite. These results underscore the critical role of dust mineralogy in influencing the SSA 720 of dust particles, as highlighted in previous studies (Li et al., 2021; Song et al., 2022, 2024). 721 However, the effects of mineralogy on lidar-derived δ and δ are comparatively smaller than the Deleted: δ Formatted: Font: Cambria Math 722 impacts from dust particle size. An important caveat to keep in mind when interpreting these Deleted: on SSA and 723 results is that the same dust CRI has been used for all three wavelengths, as mentioned earlier. 724 Dust absorption typically increases with decreasing wavelength in the visible to ultraviolet 725 spectral region, which is not accounted for in our computations. Therefore, the impacts of mineralogy on lidar properties at the 355 nm wavelength, where dust can have strong absorption, 726 727 may be underestimated. We will leave this for future studies because the spectral dependence of 728 dust CRI is still highly uncertain due to the lack of reliable observations. 729 730 731 Parameterization schemes for dust 5 Deleted: δ Formatted: Outline numbered + Level: 1 + Numbering Style: 1, 2, 3, ... + Start at: 1 + Alignment: Right + Aligned at: 0.25" + Indent at: 0.5" 732 The results in Section 3 indicate that particle size plays a dominant role in determining the dust

 δ of FIB dust particles. As shown in Section 3.1, the dust δ exhibits an asymptotic trend with

increasing size (see Figure 6b), a pattern also noted in several previous studies (Kong, S. et al.,

733

734

Deleted: δ

Deleted: δ

2022; Järvinen et al., 2016; Kemppinen et al., 2015 a, b). The robustness of this asymptotic trend inspired us to develop two parameterization schemes for δ as a function of dust size, which will be introduced in this section. This will allow us to extend the utility of the dust particle data to a larger range of sizes, as the individual particles have a limited range of size parameters. One scheme is designed for single particles, while the other is intended for ensembles of particles with a particle size distribution. We hope that these parameterization schemes can be used to efficiently estimate the δ of dust particles without resorting to time-consuming scattering simulations.

744

745

746

747

748

749

750

751

752

753

754

755

756

757

758

759

760

761

762

763

764

765

Deleted: δ

Deleted: δ

Formatted Table

Deleted: $\frac{\delta_{\infty}}{1+e^{-a(x+b)}}$

The parameterization for single particles is straightforward. To model the asymptotic trend of individual particle δ with dust particle size, we employed a sigmoid function as follows:

$$\delta_{\mathbf{v}}(x) = \frac{\delta_{\infty}}{\mathbf{v}_{1+e^{-a(x+b)}}} = \frac{0.41}{1+e^{-1.09(x-3.7)\dot{\mathbf{v}}}}$$
(10)

parameter is large. The other two parameters a_v and b_v control the shape of the sigmoid function. After a nonlinear curve fitting, we find $\delta_{\infty_v} = 0.41$, $a_v = 1.09$ and $b_v = -3.7$ ($R^2_v = 0.72$). This simple parameterization can be used to estimate the δ of a single dust particle given its size and the wavelength of interest.

The sigmoid function has three parameters: δ_{∞} is the asymptotic value of δ when the size

Deleted: ,
Deleted: ¶

Where $x = \pi r_v / \lambda$ is the particle size parameter.

Formatted: Font: 11 pt

Deleted: δ
Deleted:

Deleted:

Deleted: =

Deleted: =

Deleted: = -

Deleted: =

Formatted: Font: 11 pt

Deleted: δ

Deleted: δ

Formatted: Font: Times New Roman, Not Italic, , Highlight

Formatted: Font: 11 pt
Formatted: Font: 11 pt

Formatted: Font: 11 pt

Deleted: δ

Deleted: dln

Deleted: δ

Deleted: δ

depolarization ratio, $\langle \delta \rangle$ of a dust plume following the widely used lognormal particle size distribution $(n(r_v))$ giving us a value for δ for the ensemble of particles. To this end, we need to first make an approximation. For a given dust particle size distribution $n(r_v) = dN/d\ln r_v$, the rigorous definition of the volumetric δ is given by

Next, we will use Eq. (10) to construct a parameterization scheme for the volumetric

 $\langle \delta \rangle = \frac{1 - \langle P_{22}(\pi) \rangle / \langle P_{11}(\pi) \rangle}{1 + \langle P_{22}(\pi) \rangle / \langle P_{11}(\pi) \rangle^2}$ (11) **Deleted:** $\langle \delta \rangle = \frac{1 - \langle P_{22} \rangle / \langle P_{11} \rangle}{1 + \langle P_{22} \rangle / \langle P_{11} \rangle}$

Formatted Table

where $\langle P_{11} \rangle$ and $\langle P_{22} \rangle$ are the bulk scattering matrix elements after the averaging over $n(r_v)$

Deleted: $\langle P_{11}$ Deleted: >

For example,

787

788

789

790

791

792

793

794

795

796

797

798

799 800

801

802

Deleted: phase

Formatted: Font: 11 pt

Formatted: Font: 11 pt

Deleted: $\langle P_{11} \rangle = \frac{\int_{-\infty}^{\infty} P_{11}(r_v) C_{sca}(r_v) n(r_v) d \ln r_v}{\int_{-\infty}^{\infty} C_{sca}(r_v) n(r_v) d \ln r_v}$ $\int_{-\infty}^{\infty} C_{sca}(r_v) n(r_v) d \ln r_v$

Formatted Table

Deleted:

(12)

Formatted: Font: 11 pt

Deleted: $\langle \delta \rangle \approx \frac{\int_{-\infty}^{\infty} \delta(r_v) C_{\text{SGA}}(r_v) n(r_v) d \ln r_v}{\int_{-\infty}^{\infty} C_{\text{SGA}}(r_v) n(r_v) d \ln r_v}$

Formatted: Font: Cambria Math

Formatted: Line spacing: Multiple 1.15 li

Formatted Table

Deleted: where r_{vq} is the volume median radius,

Deleted: 2π

Deleted: λ

Deleted: δ

Deleted: The

 $\langle P_{11} \rangle = \frac{\int_{-\infty}^{\infty} P_{11}(r_v) C_{sca}(r_v) n(r_v) d\ln r_v}{\int_{-\infty}^{\infty} C_{sca}(r_v) n(r_v) d\ln r_v},$

where C_{scar} is the scattering cross section of dust particle with the size of r_v . We found that it is

difficult to use Eq. (11) to estimate $\langle \delta \rangle$, because neither $\langle P_{11} \rangle$ nor $\langle P_{22} \rangle$ can be easily

parameterized with size parameter. To avoid this difficulty, we propose the following

approximate way to estimate the $\langle \delta \rangle$ as

$$\langle \delta \rangle \approx \frac{\int_{-\infty}^{\infty} \delta(r_v) C_{sca}(r_v) n(r_v) \, d\ln r_v}{\int_{-\infty}^{\infty} C_{sca}(r_v) n(r_v) \, d\ln r_v}, \tag{13}$$

which allows us to use the simple parameterization in Eq. (10). The accuracy of this approximation will be evaluated momentarily. Here, we convert from size parameter to volume median radius through $x_{vg} = \frac{2\pi r_{vg}}{\sqrt{as}} \delta$ will vary with wavelength. Next, we need to specify the $C_{sca}(r_v)$ of single particles. Unfortunately, the size parameter span of the FIB dust samples is too small to cover the whole dust $n(r_v)$. To solve this problem, we use the TAUMdust2020 database to estimate $C_{sca}(r_v)$. TAMUdust2020 is a comprehensive database by Saito et al. (2021) that covers the scattering properties of 20 irregular hexahedral shape models over the entire practical range of particle sizes, wavelengths, and CRI of mineral dust particles. Based on the regional dust models recommended by Saito et al. (2021), an ensemble-weighted degree of sphericity of 0.7 is <u>selected</u> to represent the dust particles. For the dust CRI, we use the data from

Deleted: elected

Song et al. (2022) to interpolate the TAMUdust2020 to obtain the $C_{sca}(r_{\nu})$. In Song et al. (2022), three sets of dust CRI corresponding to the low, mean, and high concentration of hematite (Di Biagio et al., 2019) were used to compute the dust scattering properties and their direct radiative effects. Here we adopt the CRI corresponding to the mean concentration of hematite. Note that the CRI from Song et al. (2022) is spectrally dependent with increasing absorption with decreasing wavelength (see their Figure 2), which means that the 355 nm has the strongest absorption among the three lidar wavelengths considered here. Finally, for the dust $n(r_{\nu})$, we use the lognormal distribution

 $n(r_v) = \frac{dN}{d\ln(r_v)} = \frac{N_0}{\sqrt{2\pi}(\sigma_g)} exp\left[-\frac{(r_v/r_{vg})^2}{(\sigma_g)^2}\right]$ (14)

Deleted: $n(r_v) = \frac{dN}{d \ln(r_v)} = \frac{N_0}{\sqrt{2\pi}(\sigma_g)} \exp\left[-\frac{\ln^2(r_v/r_{vg})}{(\sigma_g)^2}\right],$

Formatted Table

where N_0 is a constant and r_{vg} is the volume median radius. We use a fixed standard deviation

of $\sigma_g = 0.529$, the same standard deviation of the fine mode dust from AERONET's $n(r_v)$ in

Cape Verde from Dubovik et al. (2002) shown in Figure 12, when creating the parameterization

829 <u>in Figure 11</u>.

816

817

818

819

820

821

822

823

824

825

827

828

830

831

832

833

834

835

836

TAMUdust2020 database and the lognormal $n(r_v)$ in Eq. (14), we computed the volumetric dust

Using the combination of the $\delta(x)$ parameterization in Eq. (10), the $C_{sca}(r_v)$ from the

depolarization ratio $\langle \delta \rangle$ based on the proposed approximation in Eq. (13). The result for the 532

 $nm_{\downarrow}(\delta)$ as a function of the effective size parameter is shown in Figure 11a. It is not surprising to

see that the volumetric dust depolarization ratio $\langle \delta(x_{vg}) \rangle$ resembles the $\delta(x)$ for the single

particles in terms of its size dependence. Further simplification is possible through a fitting of

Deleted: Where

Deleted: we **Deleted:** σ_a

- · · · · · · · · · · · · · · ·

Deleted: for

Deleted: used later

Formatted: Font: 11 pt

Deleted:

Deleted: $\langle \delta \rangle$

Deleted: (δ)

Deleted: $\delta \langle \delta(x_{vg}) \rangle$

Formatted: Font: 11 pt

the newly bulk averaged depolarization ratio. We find the depolarization of the FIB realistic particles are well approximated by the following hyperbolic tangent equation:

$$\langle \delta(x_{vg}) \rangle \approx 0.41 \tanh(0.14x_{vg} + 0.09)$$
 (15)

Deleted: $(\delta(x_{vg})) \approx 0.41 \tanh(0.14x_{vg} + 0.09),$

Formatted Table

wavelength of 532 nm in particular, we found that the results for the 355 nm and 1064 nm wavelengths are almost identical. This is probably because we used the same $\mathcal{L}(x)$ parameterization for all three wavelengths, and only different C_{sca} due to the use of spectrally

with an r-squared value of 0.79 as shown in Figure 11a. While this function is fitted for a

dependent CRI in Song et al. (2022). It turns out that the C_{sca} plays a minimal role in the δ value

making Eq. (15) a reasonable approximation for all three lidar wavelengths given an effective

particle size parameter, x_{vq} . This is supported by the comparison results shown in Figure 11b.

The solid lines correspond to the volumetric $\langle \delta \rangle$ for the three wavelengths predicted based on the

parameterization Eq. (15). The dotted line corresponds to the (6) of irregular hexahedral

computed based on the TAMUdust2020 database using the Song et al. (2022) dust CRI. It is

important to note that the computation for irregular hexahedral is based on the rigorous definition

of δ in Eq. (11) without any approximation. Evidently, the two sets of δ agree reasonably well

in terms of both spectral and size parameter dependencies. Interestingly, a decreasing trend was

observed for the 355 nm δ based on the irregular hexahedral when r_{vg} is larger than about 2 μ m

to 3 μm , which is not seen in either our parameterization or hexahedral results for other

wavelengths. As mentioned above, in the computation for the irregular hexahedral we used the

spectrally dependent CRI that has a higher absorption at 355 nm. Recall the result in Figure 10c

that indicates δ to decrease with dust absorption. This decreasing with size trend of δ for large

 r_{vg} is a result of stronger absorption at 355 nm, as it is reflected in a decrease in SSA for those

particles (Saito and Yang, 2021).

847

848

849

850

851

852

853

854

855

856

857

858

859

860

861

862

863

864

865

866

867

868

Deleted: δ

Deleted: δ

Deleted: >

Formatted: Font: 11 pt

Deleted: 13

Deleted: δ

Formatted: Font: 11 pt

Formatted: Font: 11 pt

Deleted: δ

Formatted: Font: 11 pt

Deleted: δ

Deleted: δ

Deleted: We believe that this

Deleted: δ

Deleted:

882

883

884

885

886

887

888

889

890

891

892

893

894

895

896

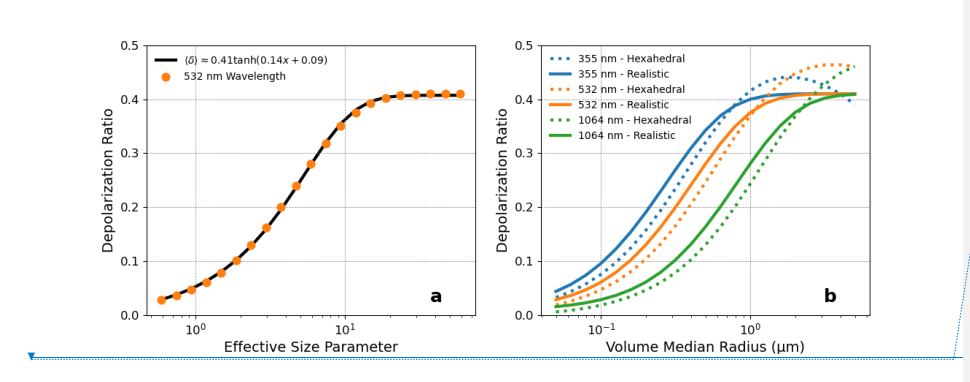


Figure 11: (a) Parameterization of realistic δ for effective size parameter using a hyperbolic tangent function. (b) Depolarization Ratio predicted for a monomodal size distribution with varying volume-equivalent median radius. The δ for realistic geometries was derived through equation 15, while hexahedral shapes used P_{II} and P_{22} parameters.

Deleted: δ

Deleted: diameter

Deleted: δ

Deleted: parameterized approximations

The utility of the simple parameterization scheme in Eq. (15) is further demonstrated in terms of simulating the spectral dependence of δ as shown in the following case. Here, we use the climatological dust $n(r_v)$ retrieved by the AERONET at Cape Verde as reported in Dubovik et al., (2002) (Figure 12a) to compute three sets of volumetric dust $\delta \delta$ for the three lidar wavelengths using the following three methods:

Deleted: δ

Deleted: >

Formatted: Font: 11 pt

1. In the first method (black solid lines in Figure 12b), dust scattering properties are based on the irregular hexahedral model from the TAMUdust2020 database. The dust CRI is spectrally dependent from the Song et al. (2022). The $\langle \delta_{\nu} \rangle$ is computed based on the rigorous definition in Eq. (11) with $\langle P_{11} \rangle$ and $\langle P_{22} \rangle$ averaged over $n(r_{\nu})$.

Formatted: Outline numbered + Level: 1 + Numbering Style: 1, 2, 3, ... + Start at: 1 + Alignment: Left + Aligned at: 0.25" + Indent at: 0.5"

Deleted: >

Formatted: Font: 11 pt

Deleted: >

Formatted: Font: 11 pt

Formatted: Font: 11 pt

Formatted: Font: 11 pt

2. In the second method (blue dashed lines in Figure 12b), same as the first method except that the $\langle \delta \rangle$ is computed based on the approximation method in Eq. (13).

Deleted:)
Formatted: Font: 11 pt
Formatted: Font: 11 pt

3. In the third method (red dotted lines in Figure 12b), the $\langle \delta \rangle$ for each wavelength is simply predicted using the parameterization in Eq. (15) by converting the x_{vg} to r_{vg} .

As such, the comparisons between the three methods enable us to assess the uncertainty associated with each step of approximation. For example, the comparison between method 1 and 2 can help us understand the uncertainty associated with the (6) computation using the approximation method in Eq. (13). The comparison of method 3 to the other two methods helps us understand the overall accuracy of our simple parameterization.

Deleted: >

Formatted: Font: 11 pt

In order to use the full $n(r_v)$ with method 3, a weighting by backscatter coefficient is utilized such that (Mamouri and Ansmann, 2014)

$$\langle \delta \rangle = \frac{\beta_f \delta_f (1 + \delta_c) + \beta_c \delta_c (1 + \delta_f)}{\beta_f (1 + \delta_c) + \beta_c (1 + \delta_f)},\tag{16}$$

Deleted: $\langle \delta \rangle = \frac{\beta_f \delta_f (1 + \delta_c) + \beta_c \delta_c (1 + \delta_f)}{\beta_f (1 + \delta_c) + \beta_c (1 + \delta_f)},$

Formatted Table

where β is calculated from the TAMUdust2020 database.

906

907

908

909

910

911

912

913

914

915

916

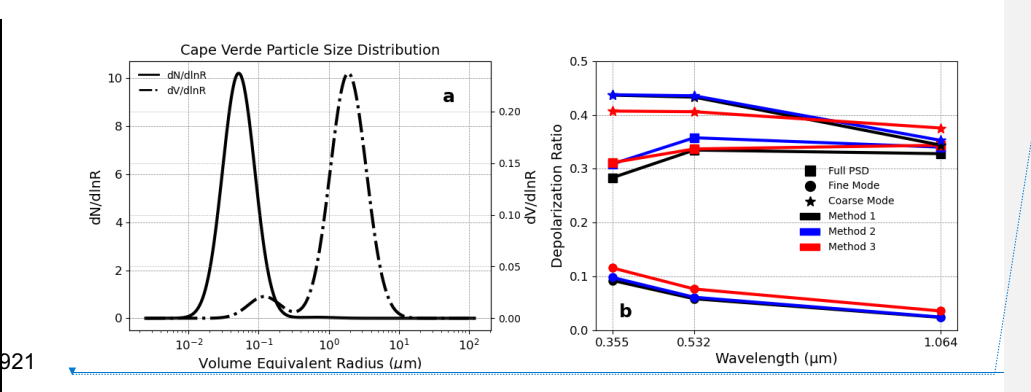
917

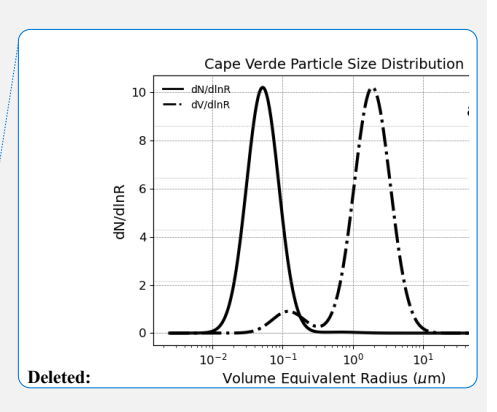
918

919

920

Formatted: Font: 11 pt





	•		Formatted: Header
926	Figure 12. (a) Dust particle size distribution for Cape Verde using AERONET, adapted from		
020	right 12. (a) Dust particle size distribution for cupe voide using 7121(01/121), adapted from		
927	Dubovik et al. (2002). (b) Depolarization Ratio of fine and coarse mode for hexahedral dust		Deleted: Vertical line indicates fine/coarse mode cutoff.
928	and FIB reconstruction using approximation methods 1, 2, and 3 as described in the text.		Deleted: previously
929			
930	The <u>resulting comparison</u> in Figure 12 <u>shows</u> all three methods simulate a substantially smaller		Deleted: comparisons shown
004			Deleted: are promising. First of all,
931	δ for the fine mode than the coarse mode. Additionally, the fine mode δ based on all three	<	Deleted: δ
932	methods exhibits a decreasing trend with wavelength which is a result of the fast-increasing trend		Deleted: Secondly
		Ì	Deleted: δ
933	of δ with dust particle size parameter for fine mode dust particles (See Figure 6). The differences		Deleted: δ
934	in the fine mode δ between the three methods are mostly smaller than 0.05, with the method 3		
935	result based on the simple parameterization scheme slightly larger than the other two methods.		
936	Finally, for the coarse mode dust δ , the results based on the simple parameterization (method 3)	************	Deleted: δ
937	are close to spectrally neutral and smaller than methods 1 and 2 for 355 and 532 nm, while the		Deleted: the other two
938	use of TAMUdust2020 decreases ♂ at 1064 nm,		
939		The same of the sa	Deleted:
940	Interestingly, the full-size distribution δs based on methods 1 and 2 exhibit an inverse "v" shape,		Deleted: δs
			Deleted: the other two
941	with the maximum at the 532nm and decreasing toward both 355 nm and 1064 nm. Such an		
942	inverse "v" shape spectral signature of dust δ has also been observed recently by (Haarig et al.,		
943	2022) over Leipzig, Germany, in February and March 2021 during a transported Sahara dust		
944	event (see their Figure 5). As aforementioned, our δ parameterization scheme using method 3		
945	and the parameterization of the FIB dust samples does not take into account the spectral		
946	dependence of dust CRI and the corresponding change of absorption. In methods 1 and 2, we		Deleted: method 2
 947	use the CRI from Song et al. (2022) which has a stronger absorption at 355 nm, which leads to	· · · · · · · · · · · · · · · · · · ·	Deleted: 3
948	a decrease of <i>§</i> from 532 nm to 355 nm. Therefore, our results indicate that the inverse "v" shape		Deleted: δ

			Formatted: Header
969	spectral signature of dust δ is a result of competing effects of dust size and absorption. The		Deleted: δ
970	decrease of δ from 532 nm to 1064 nm is the result of dust size while the decrease from 532 nm		Deleted: δ
971	to 355 nm is a result of dust absorption.		
	to 333 mm is a result of dask absorption.		
972			
973	Despite the limitation of spectrally independent CRI, the overall accuracy of our		Deleted: this
974	parameterization scheme is satisfying, partly due to the error cancellation between the		
975	overestimation of the fine mode δ and underestimation of coarse mode δ . For example, after		Deleted: δ
			Deleted: δ
976	summation of fine and coarse modes, the δ of the whole $n(r_v)$ for the 532nm wavelength is $\delta \delta \approx$		Deleted: δ
977	0.335 based on method 1, while method 3 based on our simple parameterization is $\sqrt{\delta}$ \approx 0.334.	M	Deleted: ⟩ ≈
911	0.553 based on method 1, while method 5 based on our simple parameterization is $\sqrt{\phi} \approx 0.554$.	()	Formatted: Font: 11 pt
978			Deleted: (
			Deleted: ⟩ ≈
979	Comparing the dust δ of the full $n(r_v)$ to that of fine mode δ and coarse mode δ also gives us)	Formatted: Font: 11 pt
	· ·	1	Deleted: δ
980	interesting results. Both fine and coarse modes individually decrease with wavelength despite		Deleted: δ
981	the inverse "v" shape spectral signature of the full $n(r_v)$. This characteristic is quite nicely)	Deleted: δ
L			
982	explained by an interpretation of Eq. (16). Across each wavelength, $\beta_f < \beta_c$ so $\langle \delta \rangle$ is greater		Deleted: β_f
			Deleted: β_c
983	than a simple average of both fine and coarse modes. But β_c increases with wavelength.	1/3	Deleted: δ
004		$\langle \ \ \rangle$	Formatted: Font: 11 pt
984	Therefore, despite δ_f and δ_c decreasing spectrally, δ_c has a greater weighting in the equation. In	\mathcal{L}	Formatted: Font: 11 pt
l 985	other words, more of the backscattered signal is due to larger particles as wavelength increases,	W_{j}	Formatted: Font: 11 pt
505	other words, more of the backscattered signal is due to larger particles as wavelength increases,	1//3	Deleted: δ_f
986	which are the particles exhibiting greater depolarization. Competing factors of β and δ further	/)	Deleted: δ_c
			Deleted: δ_c
987	reinforces the absorption and size impact on <u>\(\phi\)</u> . Thus, the comparisons shown in Figure 12 are	1/3	Deleted: The competing
000		//)	Deleted: δ
988	promising.		Formatted: Font: 11 pt
989)	Deleted: δ
503			
990	The utility of this parameterization likely comes from the inverse problem. Given the reliance		
991	on TAMUdust2020 for β , reconstructing the β from a $n(r_v)$ still requires use of simplified		Deleted: δ
50 1	on 171110 aust 2020 for p, reconstructing the p from a 1/19 our requires use of simplified	and the same of	Formatted: Font: 11 pt
I			

theoretical geometries for some amount of the calculation. However, given a retrieved backscattering coefficient, δ , and $n(r_v)$, using Eq. (15) and (16) creates a succinct method of retrieving β_f and β_c , separating fine and coarse fraction of dust according to Mamouri and Ansmann (2014).

Deleted: δ

Formatted: Font: 11 pt

Specifically in coarse mode analysis, there are some limitations of our study. The sigmoid parameterization leads to a very flat parameterization of δ for particles greater than 1 μ m in volume equivalent radius seen in both Figure 11b and 12b which may be further refined with larger particles, currently unavailable due to computational cost. It is also important to note our study uses a wavelength-independent refractive index based on 589 nm, causing this work to miss some spectral dependency that may cause the coarse mode differences in each wavelength when using the globally averaged refractive index (see Figure 11b). The competing effects of size and mineral composition of dust particles have been observed in studies of spectral dependence of δ (Haarig et al., 2022), which we will investigate in future studies.

Deleted: δ **Formatted:** Font: Cambria Math

Formatted: Header

Deleted: libraries

Formatted: Font: 11 pt

Deleted: has

Deleted: δ

6. Conclusions and summary

1014

1015

1016

1017

1018

1019

1020

1021

1022

1023

1024

1025

1026

1027

1028

1029

1030

1031

1032

1033

1034

1035

1036

In this study, we utilized the ADDA model to compute the scattering properties of FIB dust samples and derived the S and δ at three widely used lidar wavelengths: 355 nm, 532 nm, and 1064 nm. The advantage of this study compared to previous work is the use of realistic dust shapes reconstructed through the FIB tomography technique. The characterization of single scattering properties of these realistic samples through rigorous computational techniques should serve well as benchmark data for the dust scattering community. We investigated the dependence

Formatted: Outline numbered + Level: 1 + Numbering Style: 1, 2, 3, ... + Start at: 1 + Alignment: Right + Aligned at: 0.25" + Indent at: 0.5"

Deleted: δ

Formatted: Font: Cambria Math

of dust S and δ on dust particle size, shape, and mineral composition. The results lead to the following conclusions:

1043

1044

1045

1b46

1047

1048

1049

1050

1051

1052

1053

1054

1055

1056

1057

1058

1059

1060

1061

1062

1063

1064

1065

• Both the S and S exhibit an asymptotic trend with dust particle size: the S initially decreases while the S increases with size, before both approach their asymptotic values.

- The lidar properties were found to have only a weak dependence on effective sphericity.
- The presence of strongly absorbing minerals, such as magnetite, can greatly reduce the dust's single scattering albedo and β, while increasing S.

In addition to these scientific findings, the convergence index introduced in Section 3.3 and the

 δ parameterization schemes described in Section δ may be useful for future research on light scattering by nonspherical particles and lidar-based remote sensing. The convergence index can be used to assess the convergence of random orientation computation using the DDA method. The δ parameterization scheme in Eq. (15) can be used to estimate the δ of dust with a lognormal size distribution $n(r_v)$, which can help us understand the variation of dust size based on δ observations and the separation of fine and coarse mode dust (Mamouri and Ansmann, 2014).

Certain limitations of this study need also to be addressed, particularly regarding the parameterization scheme of Section 5. This model's parameterization leads to a flattened coarsemode in an attempt to extrapolate upon the limited size range available due to computational limits of DDA. Therefore, it may not have fully captured the optical properties for use with particularly large size parameters. Additionally, the wavelength-independent complex refractive index based on 589 nm measurements was applied to all three lidar wavelengths, simplifying the spectral differences in lidar properties, particularly at 355 nm where absorption from iron-phase minerals is more significant. Future studies on the coarse mode and spectral variation of dust

Formatted: Header

Deleted: δ

Formatted: Font: Cambria Math

Deleted: δ

Formatted: Font: Cambria Math

Formatted: Font: Cambria Math

Formatted: Outline numbered + Level: 1 + Numbering Style: Bullet + Aligned at: 0.25" + Indent at: 0.5"

Deleted: δ

Deleted: δ , especially at 355 nm

Deleted: 2

Deleted: δ

Deleted: 4

Deleted: CI

Deleted: δ

Deleted: δ

Deleted: δ

Deleted: model

Deleted: ---

-Page Break

Disclaimer 1

Certain commercial equipment, instruments, or materials, commercial or non-commercial, are identified in this paper in order to specify the experimental procedure adequately. Such identification does not imply recommendation or endorsement of any product or service by NIST, nor does it imply that the materials or equipment identified are necessarily the best available for the purpose. The opinions, recommendations, findings, and conclusions in this publication do not necessarily reflect the views or policies of NIST or the United States Government.

---Page Break

ď.

1095 lidar properties will improve the parameterization and applicability of the parameterization 1096 scheme and ability to utilize the FIB dust samples for atmospheric observations. 1097 1098 Acknowledgements: This research is supported by grants from the US National Science 1099 Foundation (AGS-2232138) and National Aeronautics and Space Administration 1100 (80NSSC24K0457). Masanori Saito is supported by the National Aeronautics and Space 1101 Administration (80NSSC24K0823). 1102 1103 1104 1105 Data Availability. The scattering properties generated for the lidar properties of the FIB dust 1106 samples presented in this work are made available under 1107 https://doi.org/10.5281/zenodo.15684438 through publication with Zenodo as a netcdf file. 1108 Readers interested in the original shape models are directed to Conny et al., 2019, for data 1109 availability. 1110 1111 Author Contributions. ZZ proposed and conceptualized the work, providing both funding 1112 acquisition and supervision of the project. All authors contributed to review & editing of the 1113 manuscript. JD helped to design the convergence index. MS and PY provided the 1114 TAMUdust2020 database for comparison to the FIB dust particles and MS provided insight into 1115 particle sphericity. JZ and QS assisted in data curation and interpretation for FIB dust lidar 1116 property results and global refractive index data. ASL and ZZ contributed to the original draft 1117 preparation of the manuscript. ASL contributed to the methodology, data collection, 1118 <u>interpretation and analysis and data visualization under ZZ supervision and project</u>
1119 <u>administration.</u>
1120

Formatted: Header

References

1121

1140

- Ansmann, A., Wandinger, U., Riebesell, M., Weitkamp, C., & Michaelis, W. (1992).
- 1123 Independent measurement of extinction and backscatter profiles in cirrus clouds by using a
- 1124 combined Raman elastic-backscatter lidar. *Applied Optics*, 31(33), 7113.
- 1125 https://doi.org/10.1364/ao.31.007113
- Baker, A. R., Kelly, S. D., Biswas, K. F., Witt, M., & Jickells, T. D. (2003). Atmospheric
- deposition of nutrients to the Atlantic Ocean. Geophysical Research Letters, 30(24).
- 1128 https://doi.org/10.1029/2003gl018518
- 1 29 Bi, L., & Yang, P. (2014a). Accurate simulation of the optical properties of atmospheric ice
- 1 1 30 crystals with the invariant imbedding T-matrix method. *Journal of Quantitative*
- 1|131 Spectroscopy and Radiative Transfer, 138, 17–35.
- 1|132 https://doi.org/10.1016/j.jqsrt.2014.01.013
- 1/133 Bi, L., & Yang, P. (2014b). High-frequency extinction efficiencies of spheroids: rigorous T-
- matrix solutions and semi-empirical approximations. *Optics Express*, 22(9), 10270.
- 1135 https://doi.org/10.1364/oe.22.010270
- 1 Bohren, C. F., & Huffman, D. R. (2008). Absorption and Scattering of Light by Small
- 1137 Particles. John Wiley & Sons.
- 1138 Burton, S. P., Ferrare, R. A., Hostetler, C. A., Hair, J. W., Rogers, R. R., Obland, M. D., et al.
- 1/139 (2012), Aerosol classification using airborne High Spectral Resolution Lidar measurements
 - methodology and examples. *Atmospheric Measurement Techniques*, 5(1), 73–98.
- 1141 https://doi.org/10.5194/amt-5-73-2012
- 1/142 Conny, J. M., & Ortiz-Montalvo, D. L. (2017). Effect of heterogeneity and shape on optical
- 1/143 properties of urban dust based on three-dimensional modeling of individual particles.
- 1 1 4 Journal of Geophysical Research: Atmospheres, 122(18), 9816–9842.
- 1|145 https://doi.org/10.1002/2017jd026488
- 1146 Conny, J. M., Collins, S. M., & Herzing, A. A. (2014). Qualitative Multiplatform
- 1 1 1 4 7 Microanalysis of Individual Heterogeneous Atmospheric Particles from High-Volume Air
- 1 | 48 Samples. Analytical Chemistry, 86(19), 9709–9716. https://doi.org/10.1021/ac5022612
- 1 49 Conny, J. M., Willis, R. D., & Ortiz-Montalvo, D. L. (2019). Analysis and Optical Modeling of
- 1 1 50 Individual Heterogeneous Asian Dust Particles Collected at Mauna Loa Observatory.
- 1|151 *Journal of Geophysical Research: Atmospheres*, 124(5), 2702–2723.

Deleted: Amiri-Farahani, A., Allen, R. J., Li, K.-F., & Chu, J.-E. (2019). The Semidirect Effect of Combined Dust and Sea Salt Aerosols in a Multimodel Analysis. *Geophysical Research Letters*, 46(17–18), 10512–10521. https://doi.org/10.1029/2019GL084590|

Formatted

Deleted: Atkinson, J. D., Murray, B. J., Woodhouse, M. T., Whale, T

Deleted: Baustian, K. J., Carslaw, K. S., et al. (2013). The importance of feldspar for ice nucleation by mineral dust in mixed-phase clouds. *Nature*, 498(7454), 355–358. https://doi.org/10.1038/nature12278

Formatted

Formatted

Deleted: 2012a). Aerosol classification using airborne High Spectral Resolution Lidar measurements – methodology and examples. *Atmospheric Measurement Techniques*, *5*(1), 73–98. https://doi.org/10.5194/amt-5-73-2012¶ Burton, S. P., Ferrare, R. A., Hostetler, C. A., Hair, J. W., Rogers, R. R., Obland, M. D., et al. (2012b). AMT -

{	Formatt	ed•	Hes	ade

1169	https://doi.org/10.1029/2018jd029387
1170	Conny, J. M., Willis, R. D., & Ortiz-Montalvo, D. L. (2020). Optical Modeling of Single Asian
1171	Dust and Marine Air Particles: A Comparison with Geometric Particle Shapes for Remote
1172	Sensing. Journal of Quantitative Spectroscopy and Radiative Transfer, 254(107197).
1173	https://doi.org/10.1016/j.jqsrt.2020.107197
1174	Creamean, J. M., Spackman, J. R., Davis, S. M., & White, A. B. (2014). Climatology of long-
1175	range transported Asian dust along the West Coast of the United States. Journal of
1176	Geophysical Research: Atmospheres, 119(21). https://doi.org/10.1002/2014jd021694
1177	Di Biagio, C.; Formenti, P.; Balkanski, Y.; Caponi, L.; Cazaunau, M.; Pangui, E.; Journet, E.;
1178	Nowak, S.; Andreae, M. O.; Kandler, K.; Saeed, T.; Piketh, S.; Seibert, D.; Williams, E. &
1179	Doussin, JF.: Complex refractive indices and single-scattering albedo of global dust
1180	aerosols in the shortwave spectrum and relationship to size and iron content, Atmospheric
1181	Chemistry and Physics, 2019, 19, 15503-15531
1182	Donovan, D. P.; van Zadelhoff, GJ. & Wang, P.: The EarthCARE lidar cloud and aerosol
1183	profile processor (A-PRO): the A-AER, A-EBD, A-TC, and A-ICE products, Atmospheric
1184	Measurement Techniques, 2024, 17, 5301-5340
1185	Draine, B. T., & Flatau, P. J. (2013). User Guide for the Discrete Dipole Approximation Code
1186	DDSCAT 7.3. arXiv.Org. Retrieved from https://arxiv.org/abs/1305.6497
1187	Draine, Bruce T., & Flatau, P. J. (1994). Discrete-Dipole Approximation For Scattering
1188	Calculations. Journal of the Optical Society of America A, 11(4), 1491.
1189	https://doi.org/10.1364/josaa.11.001491
1190	Dubovik, O., Holben, B., Eck, T. F., Smirnov, A., Kaufman, Y. J., King, M. D., et al. (2002).
1191	Variability of Absorption and Optical Properties of Key Aerosol Types Observed in
1192	Worldwide Locations. Journal of the Atmospheric Sciences, 59(3), 590-608.
1193	https://doi.org/10.1175/1520-0469(2002)059<0590:voaaop>2.0.co;2
1194	Dubovik, O., Sinyuk, A., Lapyonok, T., Holben, B. N., Mishchenko, M., Yang, P., et al.
1195	(2006). Application of spheroid models to account for aerosol particle nonsphericity in
1196	remote sensing of desert dust. Journal of Geophysical Research: Atmospheres, 111(D11).
1197	https://doi.org/10.1029/2005jd006619
1198	Evan, A. T., Dunion, J., Foley, J. A., Heidinger, A. K., & Velden, C. S. (2006). New evidence
1100	for a relationship between Atlantic transcal evalone activity and African duct outbreaks

Deleted: https://doi.org/10.1002/2014jd021694

Formatted

1201	Geophysical Research Letters, 33(19). https://doi.org/10.1029/2006GL026408		
1202	Floutsi, A. A., Baars, H., Engelmann, R., Althausen, D., Ansmann, A., Bohlmann, S., Heese,		
1203	B., Hofer, J., Kanitz, T., Haarig, M., Ohneiser, K., Radenz, M., Seifert, P., Skupin, A., Yin,		
1204	Z., Abdullaev, S. F., Komppula, M., Filioglou, M., Giannakaki, E., Stachlewska, I. S.,		
1205	Janicka, L., Bortoli, D., Marinou, E., Amiridis, V., Gialitaki, A., Mamouri, RE., Barja, B.,		
1206	and Wandinger, U. (2023). Delian – a growing collection of depolarization ratio, lidar ratio		
1207	and ångström exponent for different aerosol types and mixtures from ground-based lidar		
1208	observations. Atmospheric Measurement Techniques, 16(9):2353-2379.		
1209	Gasteiger, J., Wiegner, M., Groß, S., Freudenthaler, V., Toledano, C., Tesche, M., & Kandler,		
1210	K. (2011). Modelling lidar-relevant optical properties of complex mineral		
1211	dust aerosols. Tellus B: Chemical and Physical Meteorology, 63(4), 725.		
1212	https://doi.org/10.1111/j.1600-0889.2011.00559.x		
1213	Gasteiger, J. K. (2011, December 6). Retrieval of microphysical properties of desert dust and		
1214	volcanic ash aerosols from ground-based remote sensing (Text.PhDThesis). Ludwig-		
1215	Maximilians-Universität München. Retrieved from https://edoc.ub.uni-		
1216	muenchen.de/13786/		
1217	Goldsmith, J. (2016). High Spectral Resolution Lidar (HSRL) Instrument Handbook. Office of		
1218	Scientific and Technical Information (OSTI). https://doi.org/10.2172/1251392		
1219	Haarig, M., Ansmann, A., Engelmann, R., Baars, H., Toledano, C., Torres, B., et al. (2022).		
1220	First triple-wavelength lidar observations of depolarization and extinction-to-		
1221	backscatter ratios of Saharan dust. Atmospheric Chemistry and Physics, 22(1), 355-369.		
1222	https://doi.org/10.5194/acp-22-355-2022		
1223	Hofer, J., Ansmann, A., Althausen, D., Engelmann, R., Baars, H., Abdullaev, S. F., and		
1224	Makhmudov, A. N. (2020). Long-term profiling of aerosol light extinction, particle mass,		
1225	cloud condensation nuclei, and ice-nucleating particle concentration over Dushanbe,		
1226	Tajikistan, in central Asia. Atmospheric Chemistry and Physics, 20(8):4695-4711.		
1227	Hu, Y., Winker, D., Vaughan, M., Lin, B., Omar, A., Trepte, C., et al. (2009).		
1228	CALIPSO/CALIOP Cloud Phase Discrimination Algorithm. Journal of Atmospheric and		
1229	Oceanic Technology, 26(11), 2293-2309. https://doi.org/10.1175/2009jtecha1280.1		
1230	Huang, Y., Kok, J. F., Saito, M., & Muñoz, O. (2023). Single-scattering properties of		

ellipsoidal dust aerosols constrained by measured dust shape distributions. Atmospheric

Deleted: Field, P. R., Möhler, O., Connolly, P., Krämer, M., Cotton, R., Heymsfield, A. J., et al. (2006). Some ice nucleation characteristics of Asian and Saharan desert dust. *Atmospheric Chemistry and Physics*, 6(10), 2991–3006. https://doi.org/10.5194/acp-6-2991-2006¶

Formatted

Formatted

Deleted: Helmert, J., Heinold, B., Tegen, I., Hellmuth, O., & Wendisch, M. (2007). On the direct and semidirect effects of Saharan dust over Europe: A modeling study. *Journal of Geophysical Research: Atmospheres*, *112*(D13). https://doi.org/10.1029/2006JD007444

Formatted

 $\textbf{Deleted:}\ J., Lin, B., Minnis, P., Wang, T., Wang, X., Hu, Y$

Deleted: (2006). Satellite-based assessment of possible dust aerosols semi-direct effect on cloud water path over East Asia. *Geophysical Research Letters*, *33*(19). https://doi.org/10.1029/2006GL026561¶ Huang,

Formatted

1248	Chemistry and Physics, 23(4), 2557-2577. https://doi.org/10.5194/acp-23-2557-2023
1249	Hulst, H. C. van de (Hendrik C. (1981). Light scattering by small particles. New York: Dover
1250	Publications. Retrieved from http://archive.org/details/lightscatteringb0000huls
1251	Illingworth, A. J., Barker, H. W., Beljaars, A., Ceccaldi, M., Chepfer, H., Clerbaux, N., et al.
1252	(2015). The EarthCARE Satellite: The Next Step Forward in Global Measurements of
1253	Clouds, Aerosols, Precipitation, and Radiation. Bulletin of the American Meteorological
1254	Society, 96(8), 1311-1332. https://doi.org/10.1175/bams-d-12-00227.1
1255	Järvinen, E., Kemppinen, O., Nousiainen, T., Kociok, T., Möhler, O., Leisner, T., & Schnaiter,
1256	M. (2016). Laboratory investigations of mineral dust near-backscattering depolarization
1257	ratios. Journal of Quantitative Spectroscopy and Radiative Transfer, 178, 192-208.
1258	https://doi.org/10.1016/j.jqsrt.2016.02.003
1259	Kahnert, M., Kanngießer, F., Järvinen, E., & Schnaiter, M. (2020). Aerosol-optics model for
1260	the backscatter depolarisation ratio of mineral dust particles. Journal of Quantitative
1261	Spectroscopy and Radiative Transfer, 254(107177).
1262	https://doi.org/10.1016/j.jqsrt.2020.107177
	1 6 331
1263	Kemppinen, O., Nousiainen, T., & Jeong, G. Y. (2015 a). Effects of dust particle internal
1263	Kemppinen, O., Nousiainen, T., & Jeong, G. Y. (2015 a). Effects of dust particle internal
1263 1264	Kemppinen, O., Nousiainen, T., & Jeong, G. Y. (2015 a). Effects of dust particle internal structure on light scattering. <i>Atmospheric Chemistry and Physics</i> , 15(20), 12011–12027.
1263 1264 1265	Kemppinen, O., Nousiainen, T., & Jeong, G. Y. (2015 a). Effects of dust particle internal structure on light scattering. <i>Atmospheric Chemistry and Physics</i> , <i>15</i> (20), 12011–12027. https://doi.org/10.5194/acp-15-12011-2015
1263 1264 1265 1266	Kemppinen, O., Nousiainen, T., & Jeong, G. Y. (2015 a). Effects of dust particle internal structure on light scattering. <i>Atmospheric Chemistry and Physics</i> , <i>15</i> (20), 12011–12027. https://doi.org/10.5194/acp-15-12011-2015 Kemppinen, Osku, Nousiainen, T., & Lindqvist, H. (2015 b). The impact of surface roughness
1263 1264 1265 1266 1267	Kemppinen, O., Nousiainen, T., & Jeong, G. Y. (2015 a). Effects of dust particle internal structure on light scattering. <i>Atmospheric Chemistry and Physics</i> , <i>15</i> (20), 12011–12027. https://doi.org/10.5194/acp-15-12011-2015 Kemppinen, Osku, Nousiainen, T., & Lindqvist, H. (2015 b). The impact of surface roughness on scattering by realistically shaped wavelength-scale dust particles. <i>Journal of</i>
1263 1264 1265 1266 1267 1268	Kemppinen, O., Nousiainen, T., & Jeong, G. Y. (2015 a). Effects of dust particle internal structure on light scattering. <i>Atmospheric Chemistry and Physics</i> , <i>15</i> (20), 12011–12027. https://doi.org/10.5194/acp-15-12011-2015 Kemppinen, Osku, Nousiainen, T., & Lindqvist, H. (2015 b). The impact of surface roughness on scattering by realistically shaped wavelength-scale dust particles. <i>Journal of Quantitative Spectroscopy and Radiative Transfer</i> , <i>150</i> , 55–67.
1263 1264 1265 1266 1267 1268 1269	Kemppinen, O., Nousiainen, T., & Jeong, G. Y. (2015 a). Effects of dust particle internal structure on light scattering. <i>Atmospheric Chemistry and Physics</i> , <i>15</i> (20), 12011–12027. https://doi.org/10.5194/acp-15-12011-2015 Kemppinen, Osku, Nousiainen, T., & Lindqvist, H. (2015 b). The impact of surface roughness on scattering by realistically shaped wavelength-scale dust particles. <i>Journal of Quantitative Spectroscopy and Radiative Transfer</i> , <i>150</i> , 55–67. https://doi.org/10.1016/j.jqsrt.2014.05.024
1263 1264 1265 1266 1267 1268 1269 1270	Kemppinen, O., Nousiainen, T., & Jeong, G. Y. (2015 a). Effects of dust particle internal structure on light scattering. <i>Atmospheric Chemistry and Physics</i> , <i>15</i> (20), 12011–12027. https://doi.org/10.5194/acp-15-12011-2015 Kemppinen, Osku, Nousiainen, T., & Lindqvist, H. (2015 b). The impact of surface roughness on scattering by realistically shaped wavelength-scale dust particles. <i>Journal of Quantitative Spectroscopy and Radiative Transfer</i> , <i>150</i> , 55–67. https://doi.org/10.1016/j.jqsrt.2014.05.024 Kim, MH., Omar, A. H., Tackett, J. L., Vaughan, M. A., Winker, D. M., Trepte, C. R., et al.
1263 1264 1265 1266 1267 1268 1269 1270 1271	Kemppinen, O., Nousiainen, T., & Jeong, G. Y. (2015 a). Effects of dust particle internal structure on light scattering. <i>Atmospheric Chemistry and Physics</i> , <i>15</i> (20), 12011–12027. https://doi.org/10.5194/acp-15-12011-2015 Kemppinen, Osku, Nousiainen, T., & Lindqvist, H. (2015 b). The impact of surface roughness on scattering by realistically shaped wavelength-scale dust particles. <i>Journal of Quantitative Spectroscopy and Radiative Transfer</i> , <i>150</i> , 55–67. https://doi.org/10.1016/j.jqsrt.2014.05.024 Kim, MH., Omar, A. H., Tackett, J. L., Vaughan, M. A., Winker, D. M., Trepte, C. R., et al. (2018). The CALIPSO version 4 automated aerosol classification and lidar ratio selection
1263 1264 1265 1266 1267 1268 1269 1270 1271 1272	 Kemppinen, O., Nousiainen, T., & Jeong, G. Y. (2015 a). Effects of dust particle internal structure on light scattering. <i>Atmospheric Chemistry and Physics</i>, 15(20), 12011–12027. https://doi.org/10.5194/acp-15-12011-2015 Kemppinen, Osku, Nousiainen, T., & Lindqvist, H. (2015 b). The impact of surface roughness on scattering by realistically shaped wavelength-scale dust particles. <i>Journal of Quantitative Spectroscopy and Radiative Transfer</i>, 150, 55–67. https://doi.org/10.1016/j.jqsrt.2014.05.024 Kim, MH., Omar, A. H., Tackett, J. L., Vaughan, M. A., Winker, D. M., Trepte, C. R., et al. (2018). The CALIPSO version 4 automated aerosol classification and lidar ratio selection algorithm. <i>Atmospheric Measurement Techniques</i>, 11(11), 6107–6135.
1263 1264 1265 1266 1267 1268 1269 1270 1271 1272 1273	 Kemppinen, O., Nousiainen, T., & Jeong, G. Y. (2015 a). Effects of dust particle internal structure on light scattering. <i>Atmospheric Chemistry and Physics</i>, 15(20), 12011–12027. https://doi.org/10.5194/acp-15-12011-2015 Kemppinen, Osku, Nousiainen, T., & Lindqvist, H. (2015 b). The impact of surface roughness on scattering by realistically shaped wavelength-scale dust particles. <i>Journal of Quantitative Spectroscopy and Radiative Transfer</i>, 150, 55–67. https://doi.org/10.1016/j.jqsrt.2014.05.024 Kim, MH., Omar, A. H., Tackett, J. L., Vaughan, M. A., Winker, D. M., Trepte, C. R., et al. (2018). The CALIPSO version 4 automated aerosol classification and lidar ratio selection algorithm. <i>Atmospheric Measurement Techniques</i>, 11(11), 6107–6135. https://doi.org/10.5194/amt-11-6107-2018
1263 1264 1265 1266 1267 1268 1269 1270 1271 1272 1273 1274	 Kemppinen, O., Nousiainen, T., & Jeong, G. Y. (2015 a). Effects of dust particle internal structure on light scattering. <i>Atmospheric Chemistry and Physics</i>, 15(20), 12011–12027. https://doi.org/10.5194/acp-15-12011-2015 Kemppinen, Osku, Nousiainen, T., & Lindqvist, H. (2015 b). The impact of surface roughness on scattering by realistically shaped wavelength-scale dust particles. <i>Journal of Quantitative Spectroscopy and Radiative Transfer</i>, 150, 55–67. https://doi.org/10.1016/j.jqsrt.2014.05.024 Kim, MH., Omar, A. H., Tackett, J. L., Vaughan, M. A., Winker, D. M., Trepte, C. R., et al. (2018). The CALIPSO version 4 automated aerosol classification and lidar ratio selection algorithm. <i>Atmospheric Measurement Techniques</i>, 11(11), 6107–6135. https://doi.org/10.5194/amt-11-6107-2018 Kong, S., Sato, K., & Bi, L. (2022). Lidar Ratio–Depolarization Ratio Relations of

Kong, S. S.-K., Pani, S. K., Griffith, S. M., Ou-Yang, C.-F., Babu, S. R., Chuang, M.-T., et al.

Deleted: Johnson, B. T., Shine, K. P., & Forster, P. M. (2004). The semi-direct aerosol effect: Impact of absorbing aerosols on marine stratocumulus. *Quarterly Journal of the Royal Meteorological Society*, 130(599), 1407–1422. https://doi.org/10.1256/qj.03.61¶

Formatted

Deleted: Kanji, Z. A., Ladino, L. A., Wex, H., Boose,

Deleted: Burkert-Kohn, M., Cziczo, D. J., & Krämer, M. (2017). Overview of Ice Nucleating Particles. *Meteorological Monographs*, 58, 1.1-1.33. https://doi.org/10.1175/amsmonographs-d-16-0006.1

Formatted

Formatted

Formatted

1289	(2022). Distinct transport mechanisms of East Asian dust and the impact on downwind
1290	marine and atmospheric environments. Science of The Total Environment, 827, 154255.
1291	https://doi.org/10.1016/j.scitotenv.2022.154255
1292	Konoshonkin, A., Kustova, N., Borovoi, A., Tsekeri, A., & Gasteiger, J. (2020). Using the
1293	Physical Optics Approximation for Estimating the Light Scattering Properties of Large
1294	Dust Particles for Lidar Applications. EPJ Web of Conferences, 237, 08025.
1295	https://doi.org/10.1051/epjconf/202023708025
1296	Lau, K. M., & Kim, K. M. (2007). Cooling of the Atlantic by Saharan dust. Geophysical
1297	Research Letters, 34(23). https://doi.org/10.1029/2007GL031538
1298	Li, L., Mahowald, N. M., Miller, R. L., García-Pando, C. P., Klose, M., Hamilton, D. S., et al.
1299	(2021). Quantifying the range of the dust direct radiative effect due to source mineralogy
1300	uncertainty. Atmospheric Chemistry and Physics, 21(5), 3973-4005.
1301	https://doi.org/10.5194/acp-21-3973-2021
1302	Lin, CY., Wang, Z., Chen, WN., Chang, SY., Chou, C. C. K., Sugimoto, N., and Zhao, X.:
1303	Long-range transport of Asian dust and air pollutants to Taiwan: observed evidence and
1304	model simulation, Atmos. Chem. Phys., 7, 423-434, https://doi.org/10.5194/acp-7-423-
1305	2007, 2007.
1306	Lindqvist, H., Jokinen, O., Kandler, K., Scheuvens, D., & Nousiainen, T. (2014). Single
1307	scattering by realistic, inhomogeneous mineral dust particles with stereogrammetric shapes.
1308	Atmospheric Chemistry and Physics, 14(1), 143-157. https://doi.org/10.5194/acp-14-143-
1309	2014
1310	Liu, J., Yang, P., & Muinonen, K. (2015). Dust-aerosol optical modeling with Gaussian
1311	spheres: Combined invariant-imbedding T-matrix and geometric-optics approach. Journal
1312	of Quantitative Spectroscopy and Radiative Transfer, 161, 136–144.
1313	https://doi.org/10.1016/j.jqsrt.2015.04.003
1314	Liu, Z., Winker, D., Omar, A., Vaughan, M., Kar, J., Trepte, C., et al. (2015). Evaluation of
1315	CALIOP 532 nm aerosol optical depth over opaque water clouds. Atmospheric Chemistry
1316	and Physics, 15(3), 1265-1288. https://doi.org/10.5194/acp-15-1265-2015
1317	Liu, Zhaoyan, Sugimoto, N., & Murayama, T. (2002). Extinction-to-backscatter ratio of Asian
1318	dust observed with high-spectral-resolution lidar and Raman lidar. Applied Optics, 41(15),
1319	2760. https://doi.org/10.1364/ao.41.002760

Deleted: Lau, K. M., Kim, M. K., & Kim, K. M. (2006). Asian summer monsoon anomalies induced by aerosol direct forcing: the role of the Tibetan Plateau. *Climate Dynamics*, 26(7–8), 855–864. https://doi.org/10.1007/s00382-006-0114-z¶

Formatted

Formatted

1325 Mamouri, R. E., & Ansmann, A. (2014). Fine and coarse dust separation with polarization 1326 lidar. Atmospheric Measurement Techniques, 7(11), 3717–3735. 1327 https://doi.org/10.5194/amt-7-3717-2014 1328 Mattis, I., Ansmann, A., Müller, D., Wandinger, U., & Althausen, D. (2002). Dual-wavelength 1329 Raman lidar observations of the extinction-to-backscatter ratio of Saharan dust. 1330 Geophysical Research Letters, 29(9). https://doi.org/10.1029/2002gl014721 1331 Meng, Z., Yang, P., Kattawar, G. W., Bi, L., Liou, K. N., & Laszlo, I. (2010). Single-scattering 1332 properties of tri-axial ellipsoidal mineral dust aerosols: A database for application to 1333 radiative transfer calculations. Journal of Aerosol Science, 41(5), 501–512. 1334 https://doi.org/10.1016/j.jaerosci.2010.02.008 1335 Miller, R. L., & Tegen, I. (1998). Climate Response to Soil Dust Aerosols. Journal of Climate, 1336 11(12), 3247-3267. https://doi.org/10.1175/1520-0442(1998)011<3247:crtsda>2.0.co;2 1337 Mishchenko, M. I., & Yurkin, M. A. (2017). On the concept of random orientation in far-field 1338 electromagnetic scattering by nonspherical particles. Optics Letters, 42(3), 494. 1339 https://doi.org/10.1364/ol.42.000494 1340 Mishchenko, M. I., Travis, L. D., & Mackowski, D. W. (1996). T-matrix computations of light 1341 scattering by nonspherical particles: A review. Journal of Quantitative Spectroscopy and 1342 Radiative Transfer, 55(5), 535–575. https://doi.org/10.1016/0022-4073(96)00002-7 1343 Mishchenko, M. I., Travis, L. D., & Lacis, A. A. (2002). Scattering, Absorption, and Emission 1344 of Light by Small Particles. Cambridge University Press. 1345 Muinonen, K., Nousiainen, T., Fast, P., Lumme, K., & Peltoniemi, J. I. (1996). Light scattering 1346 by Gaussian random particles: Ray optics approximation. Journal of Quantitative 1347 Spectroscopy and Radiative Transfer, 55(5), 577-601. https://doi.org/10.1016/0022-1348 4073(96)00003-9 1349 Müller, D., Ansmann, A., Mattis, I., Tesche, M., Wandinger, U., Althausen, D., & Pisani, G. 1350 (2007). Aerosol-type-dependent lidar ratios observed with Raman lidar. Journal of 1351 Geophysical Research: Atmospheres, 112(D16). https://doi.org/10.1029/2006jd008292 1352 Myhre, G., Samset, B. H., Schulz, M., Balkanski, Y., Bauer, S., Berntsen, T. K., et al. (2013). 1353 Radiative forcing of the direct aerosol effect from AeroCom Phase II simulations. 1354 Atmospheric Chemistry and Physics, 13(4), 1853–1877. https://doi.org/10.5194/acp-13-

1355

1853-2013

1356 Omar, A. H., Winker, D. M., Vaughan, M. A., Hu, Y., Trepte, C. R., Ferrare, R. A., et al. 1357 (2009). The CALIPSO Automated Aerosol Classification and Lidar Ratio Selection 1358 Algorithm. Journal of Atmospheric and Oceanic Technology, 26(10), 1994–2014. 1359 https://doi.org/10.1175/2009JTECHA1231.1 1360 Platt, C. M. R. (1979). Remote Sounding of High Clouds: I. Calculation of Visible and Infrared 1361 Optical Properties from Lidar and Radiometer Measurements. Journal of Applied 1362 Meteorology, 18(9), 1130-1143. https://doi.org/10.1175/1520-1363 0450(1979)018<1130:rsohci>2.0.co;2 1364 Rolph, G., Stein, A., & Stunder, B. (2017). Real-time Environmental Applications and Display 1365 sYstem: READY. Environmental Modelling & Software, 95, 210–228. 1366 https://doi.org/10.1016/j.envsoft.2017.06.025 1367 Saito, M., & Yang, P. (2021). Advanced Bulk Optical Models Linking the Backscattering and 1368 Microphysical Properties of Mineral Dust Aerosol. Geophysical Research Letters, 48(17). 1369 https://doi.org/10.1029/2021gl095121 1370 Saito, M., & Yang, P. (2022). Generalization of Atmospheric Nonspherical Particle Size: 1371 Interconversions of Size Distributions and Optical Equivalence. Journal of the Atmospheric 1372 Sciences, 79(12), 3333–3349. https://doi.org/10.1175/jas-d-22-0086.1 1373 Saito, M., Yang, P., Ding, J., & Liu, X. (2021). A comprehensive database of the optical 1374 properties of irregular aerosol particles for radiative transfer simulations. Journal of the 1375 Atmospheric Sciences, 78(7), 2089–2111. https://doi.org/10.1175/jas-d-20-0338.1 1376 Song, Q., Zhang, Z., Yu, H., Kato, S., Yang, P., Colarco, P., et al. (2018). Net radiative effects 1377 of dust in the tropical North Atlantic based on integrated satellite observations and in situ 1378 measurements. Atmospheric Chemistry and Physics, 18(15), 11303–11322. 1379 https://doi.org/10.5194/acp-18-11303-2018 1380 Song, Q., Zhang, Z., Yu, H., Ginoux, P., & Shen, J. (2021). Global dust optical depth 1381 climatology derived from CALIOP and MODIS aerosol retrievals on decadal timescales: 1382 regional and interannual variability. Atmospheric Chemistry and Physics, 21(17), 13369-1383 13395. https://doi.org/10.5194/acp-21-13369-2021 1384 Song, Q., Zhang, Z., Yu, H., Kok, J. F., Di Biagio, C., Albani, S., et al. (2022). Size-resolved 1385 dust direct radiative effect efficiency derived from satellite observations. Atmospheric

Chemistry and Physics, 22(19), 13115-13135. https://doi.org/10.5194/acp-22-13115-2022

1386

	←	Formatted: Header
4bo=		
1387	Song, Q., Ginoux, P., Ageitos, M. G., Miller, R. L., Obiso, V., & García-Pando, C. P. (2024).	
1388	Modeling impacts of dust mineralogy on fast climate response. Atmospheric Chemistry and	
1389	Physics, 24(12), 7421–7446. https://doi.org/10.5194/acp-24-7421-2024	
1390	Stein, A. F., Draxler, R. R., Rolph, G. D., Stunder, B. J. B., Cohen, M. D., & Ngan, F. (2015).	
1391	NOAA's HYSPLIT Atmospheric Transport and Dispersion Modeling System. Bulletin of	
1392	the American Meteorological Society, 96(12), 2059–2077. https://doi.org/10.1175/bams-d-	
1393	14-00110.1	
1394	Sugimoto, N., Matsui, I., Shimizu, A., & Nishizawa, T. (2008). Lidar Network for Monitoring	
1395	Asian Dust and Air Pollution Aerosols. In IGARSS 2008 - 2008 IEEE International	
1396	Geoscience and Remote Sensing Symposium (Vol. 2, p. II-573-II-576).	
1397	https://doi.org/10.1109/IGARSS.2008.4779057	
1398	Tegen, I., Lacis, A. A., & Fung, I. (1996). The influence on climate forcing of mineral aerosols	Formatted
1399	from disturbed soils. Nature, 380(6573), 419-422. https://doi.org/10.1038/380419a0	
1400	Uno, I., Eguchi, K., Yumimoto, K., Takemura, T., Shimizu, A., Uematsu, M., et al. (2009).	Formatted
1401	Asian dust transported one full circuit around the globe. Nature Geoscience, 2(8), 557-560.	
1402	https://doi.org/10.1038/ngeo583	
1403	Wadell, H. (1935). Volume, Shape, and Roundness of Quartz Particles. <i>The Journal of</i>	Formatted
1404	Geology, 43(3), 250-280. https://doi.org/10.1086/624298	
1405	Welton, E. J., Campbell, J. R., Spinhirne, J. D., & Scott III, V. S. (2001). Global monitoring of	
1406	clouds and aerosols using a network of micropulse lidar systems. In SPIE Proceedings.	
1407	SPIE. https://doi.org/10.1117/12.417040	
1408	Westberry, T. K., Behrenfeld, M. J., Shi, Y. R., Yu, H., Remer, L. A., & Bian, H. (2023).	
1409	Atmospheric nourishment of global ocean ecosystems. Science, 380(6644). Retrieved from	
1410	https://www.science.org/doi/full/10.1126/science.abq5252	
1411	Winker, D. M., Vaughan, M. A., Omar, A., Hu, Y., Powell, K. A., Liu, Z., et al. (2009).	
1412	Overview of the CALIPSO Mission and CALIOP Data Processing Algorithms. Journal of	
1413	Atmospheric and Oceanic Technology, 26(11), 2310–2323.	
1414	https://doi.org/10.1175/2009jtecha1281.1	

Wu, Y., Han, Z., Nazmi, C., Gross, B., & Moshary, F. (2015). A trans-Pacific Asian dust episode and its impacts to air quality in the east coast of U.S. *Atmospheric Environment*,

106, 358-368. https://doi.org/10.1016/j.atmosenv.2015.02.013

1418 Yang, P., Ding, J., & Kattawar, G. W. (2023). Applications of Maxwell's equations to light 1419 scattering by dielectric particles. In Light, Plasmonics and Particles (pp. 133–147). 1420 Elsevier. https://doi.org/10.1016/b978-0-323-99901-4.00011-1 1421 Young, S. A., Vaughan, M. A., Garnier, A., Tackett, J. L., Lambeth, J. D., & Powell, K. A. 1422 (2018). Extinction and optical depth retrievals for CALIPSO's Version 4 data release. 1423 Atmospheric Measurement Techniques, 11(10), 5701-5727. https://doi.org/10.5194/amt-1424 11-5701-2018 1425 Yu, H., Remer, L. A., Chin, M., Bian, H., Tan, Q., Yuan, T., & Zhang, Y. (2012). Aerosols 1426 from Overseas Rival Domestic Emissions over North America. Science, 337(6094). 1427 Retrieved from https://www.science.org/doi/10.1126/science.1217576 1428 Yu, H., Chin, M., Bian, H., Yuan, T., Prospero, J. M., Omar, A. H., et al. (2015). 1429 Quantification of trans-Atlantic dust transport from seven-year (2007-2013) record of 1430 CALIPSO lidar measurements. Remote Sensing of Environment, 159, 232–249. 1431 https://doi.org/10.1016/j.rse.2014.12.010 1432 Yu, H., Chin, M., Yuan, T., Bian, H., Remer, L. A., Prospero, J. M., et al. (2015). The 1433 fertilizing role of African dust in the Amazon rainforest: A first multiyear assessment based 1434 on data from Cloud-Aerosol Lidar and Infrared Pathfinder Satellite Observations. 1435 Geophysical Research Letters, 42(6), 1984–1991. https://doi.org/10.1002/2015GL063040 1436 Yurkin, M. A., & Hoekstra, A. G. (2020). User manual for the discrete dipole approximation 1437 code ADDA 1.4.0. Retrieved from https://github.com/adda-1438 team/adda/raw/v1.4.0/doc/manual.pdf 1439 Yurkin, M.A., & Hoekstra, A. G. (2007). The discrete dipole approximation: An overview and 1440 recent developments. Journal of Quantitative Spectroscopy and Radiative Transfer, 106(1-1441 3), 558-589. https://doi.org/10.1016/j.jqsrt.2007.01.034 1442 Yurkin, Maxim A., & Hoekstra, A. G. (2011). The discrete-dipole-approximation code ADDA: 1443 Capabilities and known limitations. Journal of Quantitative Spectroscopy and Radiative 1444 Transfer, 112(13), 2234–2247. https://doi.org/10.1016/j.jqsrt.2011.01.031 1445 Zhang, X., Xu, X., Chen, H., Hu, X.-M., & Gao, L. (2022). Dust-planetary boundary layer 1446 interactions amplified by entrainment and advections. Atmospheric Research, 278, 106359.

https://doi.org/10.1016/j.atmosres.2022.106359

1447

1448